我国高压物理领域
唯一专业期刊

高压物理学报

CHINESE JOURNAL OF HIGH PRESSURE PHYSICS

高压物性第一性原理计算

2018

中国物理学会
高压物理专业委员会 主办

高 压 物 理 学 报

GAOYA WULI XUEBAO

1987 年 9 月创刊

2018 年主题专刊

·高压物性第一性原理计算·

目　　次

官方网站：www. gywlxb. cn

官方邮箱：gaoya@caep. cn

联系电话：0816-2490042

高压物理学报
CHINESE JOURNAL OF HIGH PRESSURE PHYSICS

第 32 卷 第 1 期
2018 年 2 月

高 压 物 理 学 报
CHINESE JOURNAL OF HIGH PRESSURE PHYSICS

Vol. 32, No. 1
Feb., 2018

DOI: 10.11858/gywlxb.20170606

Structure and Properties of Novel Superhard C_5N: A First-Principles Study*

LI Zihe, LIU Chao, MA Mengdong, PAN Yilong, ZHAO Zhisheng,
YU Dongli, HE Julong

(*State Key Laboratory of Metastable Materials Science and Technology, Yanshan University, Qinhuangdao* 066004, *China*)

Abstract: By using the developed particle swarm optimization algorithm on the crystal structural prediction, we proposed 6 novel carbon nitride phases with a 5 ∶ 1 stoichiometry. Their structures, stability, mechanical and electronic properties were investigated by first-principle calculations with the density functional theory. Our calculations indicate that $P\bar{6}2m$-C_5N is energetically favorable in the 6 structures. Both elastic constants and phonon-dispersion calculations show that these structures remain mechanically and dynamically stable at 0 GPa. Electronic calculations indicate that $I4_1$-C_5N is metallic while the other 5 are semiconductive. The Vickers hardness shows that all the 6 structures are superhard materials except for $I4_1$-C_5N. Formation enthalpy calculations suggest that these 6 structures can be synthesized at attainable high pressures (19−83 GPa).

Keywords: carbon nitride; first-principle calculations; superhard; high shear modulus

CLC number: O481.1; O482.1 **Document code**: A

Superhard materials (Vickers hardness $H_v \geqslant 40$ GPa) are of fundamental interest and practical importance due to their outstanding mechanical and thermal properties, such as excellent hardness, high melting point, and wear resistance. Diamond and cubic-BN (c-BN) are two types of typical superhard materials that have been widely used in industry because of the aforementioned superior properties. However, in the past few decades, the search for new superhard materials has continued. In this context, carbon nitride has become a primary candidate for low-compressibility or superhard materials due to its relatively short bond length and low bond ionicity[1]. Since the pioneering work of Liu and Cohen[2-3] that predicted hexagonal β-C_3N_4 with extraordinary hardness, considerable efforts have been devoted theoretically[4-14] and experimentally[15-24] to searching new stoichiometric carbon nitride materials with novel properties. On the theoretical side, several approaches have been applied to predict and design new superhard carbon nitrides with different stoichiometries, such as $Pnnm$-CN, $P4_2/m$-CN, α-C_3N_2, and bct-CN_2. On the experimental side, melamine, cyanamide, and other related triazine-based compounds can be used as precursors to synthesize α-, β-, and mainly g-C_3N_4 through different mechanochemical techniques in the form of thin films and nanocrystals. However, these structures have been unverified because of the limited quantity and heterogeneity of the samples, thereby resulting in exten-

* **Received date**: 2017-06-29; **Revised date**: 2017-07-08
Foundation item: National Natural Science Foundation of China (51421091, 51332005)
Biography: LI Zihe(1990—), male, doctoral student, major in research of metastable materials.
E-mail: lizihelegend@163.com
Corresponding author: HE Julong(1958—), male, doctor, professor, major in research of metastable materials.
E-mail: hjl@ysu.edu.cn

sive debates. Other structure phases of carbon nitride may exist besides C_3N_4. Recently, Stavrou et al.[25] synthesized *Pnnm*-CN using single-crystal graphite and high-pressure gas-loaded N_2 in a standard laser heated (LH) diamond anvil cell (DAC) configuration. This research achievement verifies the aforementioned assumption. Therefore, with the theoretical calculations guiding the research, other carbon nitrides with different stoichiometric measurements should be designed and calculated in the future.

1 Method

The crystal structure search is based on the global minimization of free energy surfaces merging *ab initio* total energy calculations through the particle swarm optimization (PSO) technique as implemented in the CALYPSO code[26]. First-principle calculations were performed using the CASTEP[27] code based on the density functional theory[28-29]. The exchange and correlation effects were described by the generalized gradient approximation-Perdew-Burke-Ernzerh (GGA-PBE) exchange-correlation functional[30]. Ultrasoft pseudopotentials were expanded using a plane-wave basis set with a cutoff energy of 500 eV, and a k-point spacing ($2\pi\times0.4$ nm^{-1}) was assigned to generate Monkhorst-Pack k-point grids for Brillouin zone sampling[31]. Structural optimization using the BFGS minimization method was performed until the energy change of each atom was less than 5×10^{-6} eV, the forces on atoms were less than 0.1 eV·nm^{-1}, and all the stress components were less than 0.02 GPa[32]. The phonon modes of the equilibrium crystal structure obtained after structural relaxation were calculated using the finite displacement theory[33]. For the calculated phonon dispersion in reciprocal space, the high symmetry point coordinates were G (0,0,0), A (0,0,0.5), H (−0.33,0.67,0.50), K (−0.33, 0.67,0), M (0,0.5,0), and L (0,0.5,0.5). The polycrystalline bulk modulus, shear modulus, Young's modulus, and Poisson's ratio were estimated using the Voigt-Reuss-Hill approximation[34].

2 Results and Discussions

2.1 Crystal Structure

Through the CALYPSO code, crystal structure searches were performed with a cell size of up to 48 atoms (40 C atoms and 8 N atoms) within a pressure range of 0−70 GPa. Analysis of the predicted structures gives us a shortlist of candidate structures with space groups $P\bar{6}2m$ (2 formula units per cell), $I4_1$ (4 formula units per cell), $Pbcn$ (8 formula units per cell), $P6_3cm$ (8 formula units per cell), $P2_12_12_1$ (8 formula units per cell) and $Pna2_1$ (8 formula units per cell), respectively, as shown in Fig. 1. In these novel structures, $I4_1$-C_5N and $P6_3cm$-C_5N are sp^2-sp^3 hybridized while the other 4 are all sp^3 hybridized phases. The N atoms and the 3 bonded C atoms are almost coplanar in the $P\bar{6}2m$-C_5N, $I4_1$-C_5N, $Pbcn$-C_5N and $P6_3cm$-C_5N structures, while they form a tetrahedron in the $Pna2_1$-C_5N. Furthermore, in the $P2_12_12_1$-C_5N structure, these 2 kinds of N atoms both exist. The optimized lattice parameters, atom positions, space groups, densities and cell volumes of the 6 types of C_5N are obtained and listed in Table 1.

2.2 Stability Analysis

To explore the thermodynamic stability for further experimental synthesis, the formation enthalpy of the 6 novel C_5N structures with respect to the separate phases is quantified by $\Delta H_f = E_{C_5N} - 5E_C - (1/2)E_{N_2}$, where E_{C_5N} is the ground state enthalpy of the new C_5N phase, E_C is the energy of C atom obtained from graphite, and E_{N_2} is the total energy of the stable molecular α phase of nitrogen reported earlier[35]. The calculated formation enthalpy of these C_5N structures as functions of pressure is shown in Fig. 2.

Table 1　Structure parameters of the newly predicted C_5N

Phase	Crystal system	Space group	Atoms positions	Lattice parameters/nm	Density/(g·cm^{-3})	Cell volume/nm^3
$P\bar{6}2m$-C_5N	Hexagonal	$P\bar{6}2m$	C: 6*i* (0.668 6, 0, 0.685 1) C: 4*h* (0.333 3, 0.666 7, 0.184 6) N: 2*e* (0, 0, 0.252 0)	*a*=0.426 10 *c*=0.449 04	3.483 66	0.070 605 6
$I4_1$-C_5N	Tetragonal	$I4_1$	C: 8*b* (1.392 2, 0.304 7, 0.221 3) C: 8*b* (0.888 8, 0.302 5, 0.565 1) C: 4*a* (0.500 0, −0.500 0, 0.664 9) N: 4*a* (0.500 0, −0.500 0, 0.371 7)	*a*=0.565 54 *c*=0.461 99	3.329 25	0.147 761
Pbcn-C_5N	Orthorhombic	*Pbcn*	C: 8*d* (0.839 4, 1.185 9, 0.665 3) C: 8*d* (0.944 3, 0.510 5, 1.378 0) C: 8*d* (0.727 2, 1.419 3, 1.396 7) C: 8*d* (1.416 5, 1.445 1, 0.543 3) C: 4*c* (0.500 0, 1.349 1, 0.750 0) C: 4*c* (0.500 0, 0.812 5, 0.750 0) N: 8*d* (1.315 9, 0.707 9, 1.403 3)	*a*=0.692 19 *b*=0.759 85 *c*=0.552 51	3.385 59	0.290 603
$P6_3cm$-C_5N	Hexagonal	$P6_3cm$	C: 12*d* (0.154 9, 0.410 3, 0.866 7) C: 12*d* (0.409 9, 0.154 2, 0.693 1) C: 6*c* (0.782 2, 0, 0.648 6) C: 4*b* (0.333 3, 0.666 7, 0.124 7) C: 4*b* (0.333 3, 0.666 7, 0.941 3) C: 2*a* (0, 0, 0.414 3) N: 6*c* (0.784 7, 0, 0.910 1) N: 2*a* (0, 0, 0.151 9)	*a*=0.615 46 *c*=0.943 32	3.179 45	0.309 444
$P2_12_12_1$-C_5N	Orthorhombic	$P2_12_12_1$	C: 4*a* (−0.466 0, 0.364 8, 0.025 1) C: 4*a* (−0.035 6, 0.414 0, 0.784 6) C: 4*a* (0.408 2, 0.755 3, 0.494 3) C: 4*a* (−0.302 6, 0.231 6, 0.496 5) C: 4*a* (−0.341 4, 0.702 3, 0.989 9) C: 4*a* (0.432 1, 0.397 5, 0.519 8) C: 4*a* (−0.445 0, 0.692 8, 0.481 2) C: 4*a* (0.124 6, 0.438 9, 0.522 9) C: 4*a* (0.313 1, 0.924 8, 0.470 3) C: 4*a* (−0.072 2, 0.990 7, 0.477 8) N: 4*a* (−0.253 6, 0.868 1, 0.988 5) N: 4*a* (−0.286 0, 0.600 1, 0.055 7)	*a*=0.804 49 *b*=1.408 89 *c*=0.256 59	3.383 0	0.290 827
$Pna2_1$-C_5N	Orthorhombic	$Pna2_1$	C: 4*a* (0.626 2, 0.290 9, 0.796 6) C: 4*a* (0.666 9, 0.499 9, 0.848 8) C: 4*a* (0.445 7, 0.119 1, 0.129 6) C: 4*a* (0.351 3, 0.008 5, 0.110 2) C: 4*a* (0.441 2, 0.811 5, 0.859 2) C: 4*a* (0.103 0, 0.160 9, 0.066 6) C: 4*a* (0.975 7, 0.200 5, 0.331 8) C: 4*a* (0.261 7, 0.152 7, 0.541 9) C: 4*a* (0.748 6, 0.623 5, 0.458 7) C: 4*a* (0.311 9, 0.039 9, 0.607 6) N: 4*a* (0.322 5, 0.479 6, 0.860 4) N: 4*a* (0.771 2, 0.200 0, 0.776 8)	*a*=0.402 99 *b*=1.402 05 *c*=0.516 40	3.372 0	0.291 776

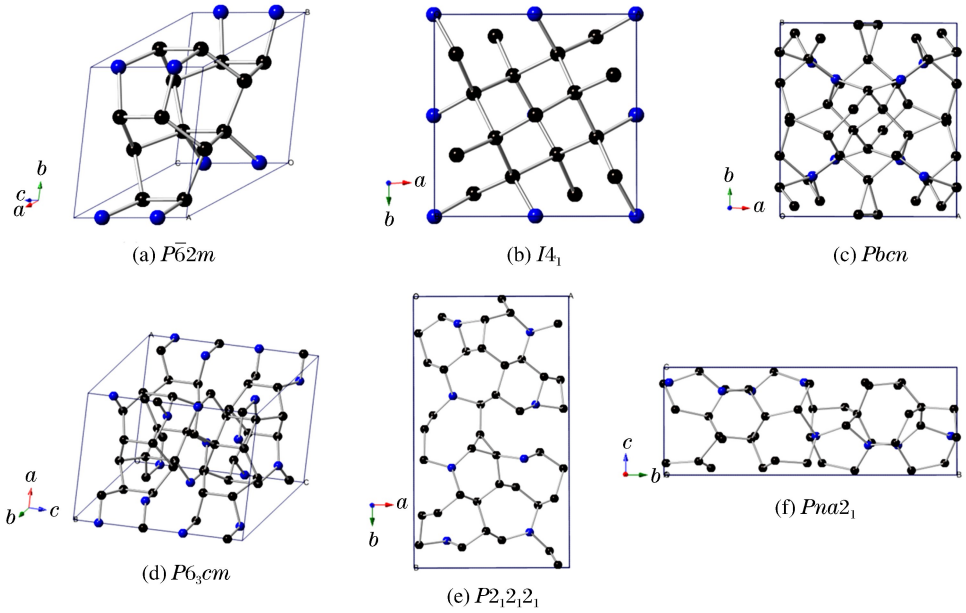

Fig. 1　Predicted structure graphs of C_5N (The spheres in color black and blue represent C and N atoms, respectively.)

From Fig. 2, the formation enthalpies suggest that these C_5N phase is metastable at 0 GPa because of its positive value, which is similar to that of diamond and c-BN. Meanwhile, as the pressure rises from 19 GPa to 83 GPa, all these 6 phases gradually become thermodynamically stable. Moreover, the use of high temperature is a classical way to improve both the diffusion processes and the reactivity of precursors for the material synthesis of bulk forms or thin films. That is, if we use graphite and nitrogen as precursors for condensed carbon nitrides at high pressure, then these C_5N phases may be synthesized at readily attainable pressures and temperatures. Furthermore, our phonon calculations have verified that these 6 C_5N is dynamically stable as evidenced by the absence of any imaginary frequency in the whole Brillouin zone at ambient pressure (see Fig. 3).

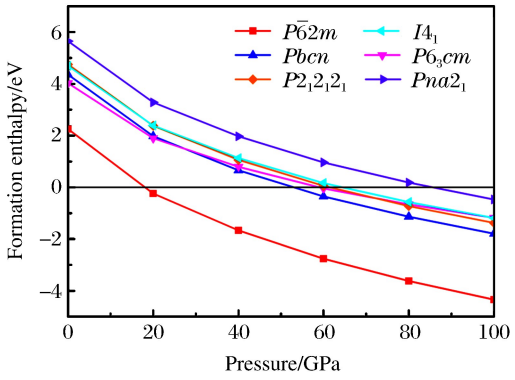

Fig. 2　Formation enthalpy of the newly predicted C_5N phases relative to graphite and nitrogen as a function of pressure

To evaluate the mechanical stability of a crystal structure, the elastic constants of a crystal should satisfy the generalized elastic stability criteria. For a hexagonal crystal, 5 independent elastic constants, namely, C_{11}, C_{33}, C_{44}, C_{12}, and C_{13}, should obey the following generalized Born mechanical stability criteria[35]: $C_{44}>0$, $C_{11}>|C_{12}|$, and $(C_{11}+2C_{12})C_{33}>2C_{13}^2$. For a tetragonal crystal, there are 6 independent elastic constants, namely, C_{11}, C_{33}, C_{44}, C_{66}, C_{12}, and C_{13}, and the corresponding mechanical stability criterion is given by: $C_{ij}>0$ $(i=j=1-6)$, $C_{11}-C_{12}>0$, $C_{11}+C_{33}-2C_{13}>0$, $2(C_{11}+C_{12})+C_{33}+4C_{13}>0$. For an orthorhombic crystal, there are 9 independent elastic constants, namely, C_{11}, C_{22}, C_{33}, C_{44}, C_{55}, C_{66}, C_{12}, C_{13} and C_{23}, and the corresponding mechanical stability criterion is as follow: $C_{ij}>0$

($i=j=1-6$), $C_{11}+C_{22}+C_{33}+2(C_{12}+C_{13}+C_{23})>0$, $C_{11}+C_{22}-2C_{12}>0$, $C_{11}+C_{33}-2C_{13}>0$, $C_{22}+C_{33}-2C_{23}>0$. The calculated elastic constant values of C_5N phases by the strain-stress method are listed in Table 2. According to the above criteria, the calculation results indicate that these novel structures are all mechanically stable under ambient pressure.

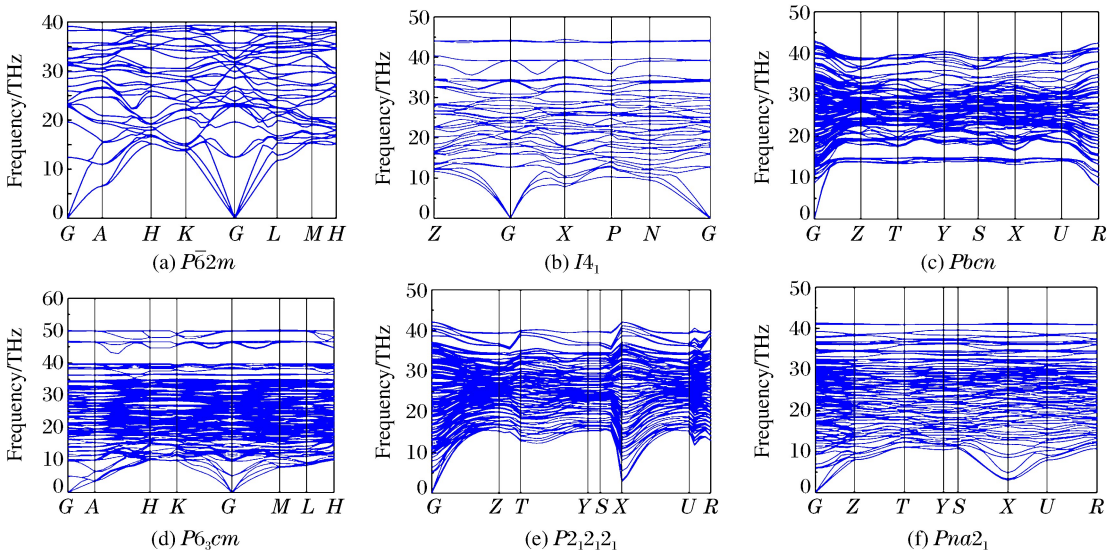

Fig. 3　Phonon dispersion spectrum at 0 GPa

Table 2　Calculated independent elastic constants C_{ij} of the newly predicted C_5N

Phase	C_{11}/GPa	C_{22}/GPa	C_{33}/GPa	C_{44}/GPa	C_{55}/GPa	C_{66}/GPa	C_{12}/GPa	C_{13}/GPa	C_{15}/GPa	C_{23}/GPa	C_{25}/GPa
P$\bar{6}$2m-C_5N	1 194		930	252			113	18			
$I4_1$-C_5N	649		931	244		247	244	75			
Pbcn-C_5N	762	663	822	382	360	364	190	83	165		
P6$_3$cm-C_5N	873		490	192			170	35			
P2$_1$2$_1$2$_1$-C_5N	902	847	893	299	341	347	120	93	40	902	847
Pna2$_1$-C_5N	891	659	736	289	372	324	86	153	149	891	659

2.3　Properties

Based on the Voigt-Reuss-Hill approximation, bulk modulus (B), shear modulus (G), Young's modulus (E) and Poisson's ratio (σ) can be obtained from the calculated elastic constants. The calculated B, G, E and σ of the newly predicted C_5N are listed in Table 3. Bulk modulus is a measure of the resistance against volume change imposed by the applied pressure, while shear modulus represents the resistance to the shear deformation against external forces, which indicates the resistance to the change in the bond angle. The hardness is deduced from the size of the indentation after deformation. A superhard material typically requires a high bulk modulus to support the volume decrease created by the applied pressure and a high shear modulus so that the material will not deform in a direction different from that of the applied load. From Table 3, it is obvious that both B and G of P$\bar{6}$2m-C_5N are the largest among the 6 new structures, indicating it can withstand stronger compression and higher shear stress than the other structures.

The relative directionality of covalent bonds of materials also has an important effect on their hardness and mechanical properties, which can be determined by the G/B ratio[36]. Table 3 shows that the G/B ratio of $P2_12_12_1$-C_5N (1.014) is higher than that of the other 5 C_5N phases, thereby suggesting the stronger directional bonding feature of $P2_12_12_1$-C_5N. The relative orientation of material bonding also has an important effect on their hardness. Young's modulus (E) is defined as the ratio between stress and strain and is used to provide a measure of stiffness of the solid, i. e. , the larger the value of E, the stiffer the material is. Poisson's ratio (σ) quantifies the stability of the crystal against shear. Except for $I4_1$-C_5N, the fairly large value of E and small Poisson's ratio indicate that the other 5 C_5N phases are rather stiff and relatively stable against shear. Thus, the preceding results reveal that these new C_5N phases are potential candidates for superhard materials and this will be confirmed by our following calculations of the Vickers hardness.

Table 3　Calculated bulk modulus B, shear modulus G, Young's modulus E and Vickers hardness H_v of the newly predicted C_5N (Also shown are G/B ratio and Poisson's ratio σ)

Phase	B/GPa	G/GPa	E/GPa	σ	G/B	H_v/GPa
$P\bar{6}2m$-C_5N	397	394	888	0.127	0.992	62.5
$I4_1$-C_5N	335	238	577	0.213	0.711	30.0
$Pbcn$-C_5N	347	338	765	0.133	0.973	55.0
$P6_3cm$-C_5N	286	267	611	0.144	0.934	44.5
$P2_12_12_1$-C_5N	349	354	794	0.121	1.014	59.6
$Pna2_1$-C_5N	338	321	731	0.139	0.949	51.6

The electronic structure determines the fundamental physical and chemical properties of materials. The calculated electronic band structure of the new predicted C_5N phases at 0 GPa are presented in Fig. 4. From Fig. 4, we can find that $I4_1$-C_5N are metallic, $Pbcn$-C_5N and $Pna2_1$-C_5N are direct-bandgap semiconductors while $P\bar{6}2m$-C_5N, $P6_3cm$-C_5N and $P2_12_12_1$-C_5N are indirect-bandgap semiconductors. All these 5 semiconductors are narrow bandgap semiconductors and their bandgaps are 1.131, 0.971, 2.312, 0.796 and 1.088 eV, respectively. The narrow bandgap feature suggests that they

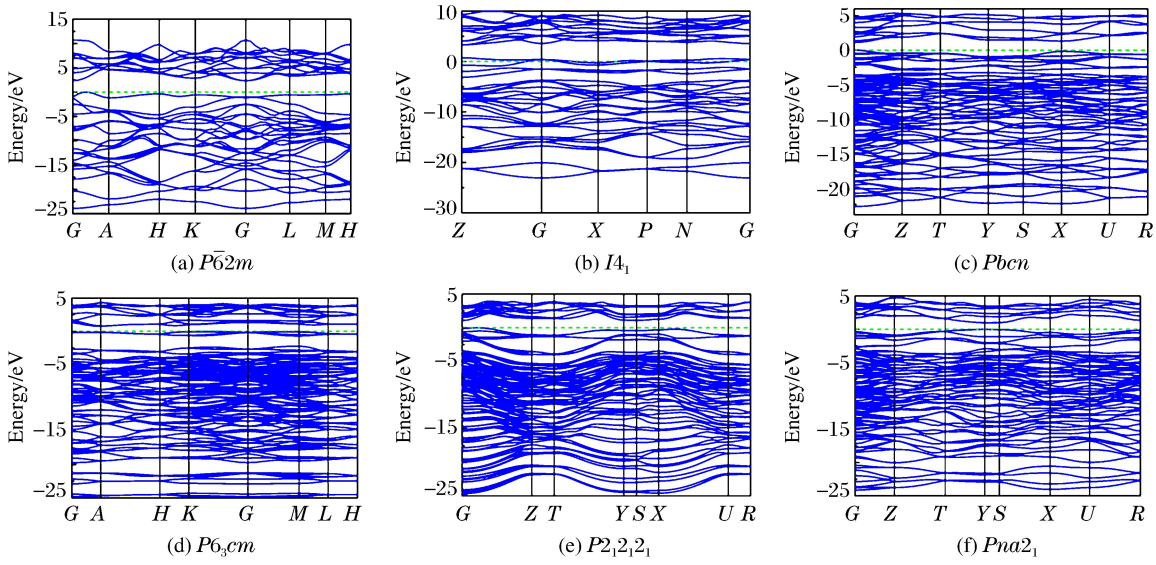

Fig. 4　Electronic band structures of newly predicted C_5N at 0 GPa

may be used as photocatalyst. In addition, the direct bandgap feature indicates *Pbcn*-C_5N and $Pna2_1$-C_5N are promising materials for the solar cell or photography industry.

In order to figure out the theoretical Vickers hardness of the new C_5N structures, we employed the macroscopic hardness model proposed by Chen *et al*.[37] and revised by Tian *et al*.[38]. The formula is $H_v(\mathrm{GPa}) = 0.92k^{1.137}G^{0.708}$, where k is the Pugh modulus ratio and equal to G/B. The results are shown in Table 3. We can find that these new compounds are superhard materials except for $I4_1$-C_5N and the hardness of $P\bar{6}2m$-C_5N and $P2_12_12_1$-C_5N are even close to that of c-BN.

3 Conclusions

In summary, using the developed PSO technique on the crystal structure prediction, we predicted 6 types of C_5N structures, and systematically investigated their geometry structures, stability, electronic and mechanical properties by first-principle calculations based on the density functional theory. All these new phases are metastable at ambient pressure but become energetically more stable than graphite and N_2 under high pressures (19－83 GPa). In addition, they are proved to be mechanically and dynamically stable at ambient pressure by computing their elastic constants and phonon dispersions. Furthermore, except for $I4_1$-C_5N, the other 5 phases are superhard semiconductors as well. The present work has great implications for designing and researching novel superhard materials.

References:

[1] LÉGER J-M, HAINES J. The search for superhard materials [J]. Endeavour, 1997, 21(3): 121-124.

[2] LIU A Y, COHEN M L. Prediction of new low compressibility solids [J]. Science, 1989, 245(4920): 841-842.

[3] LIU A Y, COHEN M L. Structural properties and electronic structure of low-compressibility materials: β-Si_3N_4 and hypothetical β-C_3N_4 [J]. Physical Review B, 1990, 41(15): 10727-10734.

[4] CÔTÉAND M, COHEN M L. Carbon nitride compounds with 1∶1 stoichiometry [J]. Physical Review B, 1997, 55(9): 5684.

[5] HALES J, BARNARD A S. Thermodynamic stability and electronic structure of small carbon nitride nanotubes [J]. Journal of Physics: Condensed Matter, 2009, 21(14): 144203.

[6] KIM E, CHEN C, KÖHLER T, et al. Tetragonal crystalline carbon nitrides: theoretical predictions [J]. Physical Review Letters, 2001, 86(4): 652-655.

[7] KIM E, CHEN C. Stability of tetragonal crystalline carbon nitrides: the nitrogen content dependence [J]. Physics Letters A, 2001, 282(6): 415-420.

[8] HART J N, CLAEYSSENS F, ALLAN N L, et al. Carbon nitride: *ab initio* investigation of carbon-rich phases [J]. Physical Review B, 2009, 80(17): 174111.

[9] SANDRÉ É, PICKARD C J, COLLIEX C. What are the possible structures for CN_x compounds? The example of C_3N [J]. Chemical Physics Letters, 2000, 325(1/2/3): 53-60.

[10] TIAN F, WANG J, HE Z, et al. Superhard semiconducting C_3N_2 compounds predicted via first-principles calculations [J]. Physical Review B, 2008, 78(23): 235431.

[11] WANG X. Polymorphic phases of sp^3-hybridized superhard CN [J]. The Journal of Chemical Physics, 2012, 137(18): 184506.

[12] ZHANG M, WEI Q, YAN H, et al. A novel superhard tetragonal carbon mononitride [J]. The Journal of Physical Chemistry C, 2014, 118(6): 3202-3208.

[13] LI Q, LIU H, ZHOU D, et al. A novel low compressible and superhard carbon nitride: body-centered tetragonal CN_2 [J]. Physical Chemistry Chemical Physics, 2012, 14(37): 13081-13087.

[14] XU Y, GAO S P. Band gap of C_3N_4 in the GW approximation [J]. International Journal of Hydrogen Energy, 2012, 37(15): 11072-11080.

[15] GUO L P, CHEN Y, WANG E G, et al. Identification of a new tetragonal C-N phase [J]. Journal of Crystal Growth, 1997, 178(4): 639-644.

[16] SEKINE T, KANDA H, BANDO Y, et al. A graphitic carbon nitride [J]. Journal of Materials Science Letters, 1990, 9(12): 1376-1378.

[17] STEVENS A J, KOGA T, AGEE C B, et al. Stability of carbon nitride materials at high pressure and temperature [J]. Journal of the American Chemical Society, 1996, 118(44): 10900-10901.

[18] STEVENS A J, AGEE C B, LIEBER C M. High-pressure chemistry of carbon nitride materials [J/OL]. MRS Online Proceedings Library, 1997, 499: 309(2011-02-01)[2017-06-29]. https://doi.org/10.1557/PROC-499-309.

[19] CHEN Y A, GUO L, WANG E G. Alpha beta experimental evidence for alpha- and beta-phases of pure crystalline C_3N_4 in films deposited on nickel substrates [J]. Philosophical Magazine Letters, 1997, 75(3): 155-162.

[20] NIU C, LU Y Z, LIEBER C M. Experimental realization of the covalent solid carbon nitride [J]. Science, 1993, 261(5119): 334-337.

[21] YU K M, COHEN M L, HALLER E E, et al. Observation of crystalline C_3N_4 [J]. Physical Review B, 1994, 49(7): 5034-5037.

[22] YIN L W, LI M S, LIU Y X, et al. Synthesis of beta carbon nitride nanosized crystal through mechanochemical reaction [J]. Journal of Physics: Condensed Matter, 2003, 15(2): 309-314.

[23] GUO Q, XIE Y, WANG X, et al. Characterization of well-crystallized graphitic carbon nitride nanocrystallites via a benzene-thermal route at low temperatures [J]. Chemical Physics Letters, 2003, 380(1/2): 84-87.

[24] JÜRGENS B, IRRAN E, SENKER J, et al. Melem (2,5,8-triamino-tri-*s*-triazine), an important intermediate during condensation of melamine rings to graphitic carbon nitride: synthesis, structure determination by X-ray powder diffractometry, solid-state NMR, and theoretical studies [J]. Journal of the American Chemical Society, 2003, 125(34): 10288-10300.

[25] STAVROU E, LOBANOV S, DONG H, et al. Synthesis of ultra-incompressible sp^3-hybridized carbon nitride with 1∶1 stoichiometry [J]. Chemistry of Materials, 2016, 28(19): 6925-6933.

[26] WANG Y, LÜ J, ZHU L, et al. Crystal structure prediction via particle-swarm optimization [J]. Physical Review B, 2010, 82(9): 094116.

[27] SEGALL M D, PHILIP J D L, PROBERT M J, et al. First-principles simulation: ideas, illustrations and the CASTEP code [J]. Journal of Physics: Condensed Matter, 2002, 14(11): 2717-2744.

[28] KOHN W, SHAM L J. Self-consistent equations including exchange and correlation effects [J]. Physical Review A, 1965, 140(4): 1133-1138.

[29] HOHENBERG P, KOHN W. Inhomogeneous electron gas [J]. Physical Review B, 1964, 136(3): 864-871.

[30] JONES R O, GUNNARSSON O. The density functional formalism, its applications and prospects [J]. Reviews of Modern Physics, 1989, 61(3): 689-746.

[31] MONKHORST H J, PACK J D. Special points for Brillouin-zone integrations [J]. Physical Review B, 1976, 13(12): 5188-5192.

[32] FISCHER T H, ALMLOF J. General methods for geometry and wave function optimization [J]. The Journal of Physical Chemistry, 1992, 96(24): 9768-9774.

[33] CLARK S J, SEGALL M D, PICKARD C J, et al. First principles methods using CASTEP [J]. Zeitschrift für Kristallographie-Crystalline Materials, 2005, 220(5/6): 567-570.

[34] HILL R. The elastic behaviour of a crystalline aggregate [J]. Proceedings of the Physical Society: Section A, 1952, 65(5): 349.

[35] VENABLES J A, ENGLISH C A. Electron diffraction and the structure of α-N_2 [J]. Acta Crystallographica Section B: Structural Science, Crystal Engineering and Materials, 1974, 30: 929-935.

[36] WU Z J, ZHAO E J, XIANG H P, et al. Crystal structures and elastic properties of superhard IrN_2 and IrN_3 from first principles [J]. Physical Review B, 2007, 76(5): 054115.

[37] CHEN X Q, NIU H, LI D, et al. Modeling hardness of polycrystalline materials and bulk metallic glasses [J]. Intermetallics, 2011, 19(9): 1275-1281.

[38] TIAN Y, XU B, ZHAO Z. Microscopic theory of hardness and design of novel superhard crystals [J]. International Journal of Refractory Metals and Hard Materials, 2012, 33: 93-106.

新型超硬 C_5N 晶体结构及性能的第一性原理研究

李子鹤, 刘　超, 马梦东, 潘益龙, 赵智胜, 于栋利, 何巨龙

(燕山大学亚稳材料制备技术与科学国家重点实验室, 河北 秦皇岛　066004)

摘要: 通过使用在晶体结构预测方面成熟的粒子群优化算法, 提出了 6 种化学计量比为 5∶1 的氮化碳新相。采用基于密度泛函理论的第一性原理计算研究它们的结构、稳定性、机械性能和电子性质。计算结果表明, 在提出的 6 种结构中, $P\bar{6}2m$-C_5N 是能量最稳定的。弹性常数和声子谱计算表明, 这些结构在 0 GPa 时是机械稳定和动力学稳定的。电子计算显示, $I4_1$-C_5N 是金属性的, 而其他 5 种结构是半导体。维氏硬度计算表明, 除 $I4_1$-C_5N 外, 其余氮化碳都为超硬材料。通过形成焓计算, 分析认为这 6 种结构能在目前实验所能达到的高压下合成(19～83 GPa)。

关键词: 氮化碳; 第一性原理计算; 超硬; 高剪切强度

中图分类号: O481.1; O482.1　　**文献标识码**: A

高压物理学报
CHINESE JOURNAL OF HIGH PRESSURE PHYSICS

第 32 卷 第 2 期
2018 年 4 月

高 压 物 理 学 报
CHINESE JOURNAL OF HIGH PRESSURE PHYSICS

Vol. 32, No. 2
Apr., 2018

DOI: 10.11858/gywlxb.20170640

高压下立方 BC_3 的力学和热力学性质*

常少梅

(宝鸡文理学院物理与光电技术学院,陕西 宝鸡 721016)

摘要:采用基于密度泛函理论的第一性原理赝势方法,系统地研究了立方 BC_3 在常压和高压下的晶格常数和力学性质,包括弹性常数、弹性模量和力学各向异性。利用准简谐近似下的德拜模型研究了高温高压条件下的热力学性质。研究结果表明:常压下立方 BC_3 具有较大的弹性模量和力学各向异性;高压下,立方 BC_3 的晶格常数、弹性常数和弹性模量显著增加。热力学性质的计算结果表明,立方 BC_3 具有较高的德拜温度,其摩尔定容热容和摩尔定压热容在高温高压条件下呈现明显的变化。立方 BC_3 的德拜温度随着压力的增大而增加,但随着温度的增大而明显减小。

关键词:第一性原理;立方 BC_3;高压;力学性质;热力学性质

中图分类号:O521.21 **文献标识码**:A

超硬材料是指维氏硬度(Vickers Hardness)超过 40 GPa 的一类功能材料。超硬材料可以作为研磨、抛光、切割工具以及抗磨损和保护涂层材料,其合成和设计一直都是材料学科中非常令人关注的领域[1-4]。典型的超硬材料有金刚石和硬度略低于金刚石的立方氮化硼。尽管传统的超硬材料金刚石硬度可达 115 GPa[5],然而其热稳定性较低,化学惰性较差,因此其工业应用受到很大的限制。替代材料立方氮化硼虽具有良好的化学惰性和热稳定性,但是其硬度(62 GPa[6])远小于金刚石,而且实验中很难合成大块的单晶。有鉴于此,设计和合成具有高硬度、良好热稳定性和化学惰性的新型超硬材料是材料学科中亟待解决的问题。目前,对超硬材料的研究主要集中于两类化合物:一类是由轻元素(B、C、N、O)构成的键长短、键密度大、离子性小的强共价化合物,例如 BC_3[7]、BC_5[8]、BC_2N[9]、B_6O[10];另一类是由具有高价电子密度的过渡金属原子和轻元素形成的化合物,如 ReB_2[11]、FeB_4[12]、PtN_2[13]、Os_2C[14]。

由硼元素和碳元素组成的硼碳化合物具有许多优点,如超高的硬度、很好的抗氧化能力、优良的电子性质等,因此研究者试图从硼碳化合物中寻找潜在的超硬材料。实验上,采用金刚石对顶砧高压装置,结合激光直接加热的方法,Solozhenko 等[8]在压力 24 GPa 和温度 2 200 K 的条件下,成功合成了维氏硬度高达 71 GPa 的立方 BC_5,研究表明立方 BC_5 是良好的研磨和耐高温材料。Zinin 等[7]在压力 39 GPa 和温度 2 200 K 的条件下,合成了立方结构的 BC_3,电子能量损失谱的实验证明,其内部原子全部都是 sp^3 杂化成键。然而,由于 B 原子和 C 原子的原子序数较小且相邻,其电子和原子核的散射截面非常相似,因此很难通过常规的 X 射线衍射等手段确定这些硼碳化合物的晶体结构及其 B、C 原子占位[15]。目前,密度泛函理论的日益成熟和结构预测技术[16-18]的不断发展使通过理论方法确定晶体结构成为现实,不依赖任何经验参数,仅仅利用材料的化学组分和给定外界条件(如压强),就能够确定材料在给定外界条件下的晶体结构。Zhang 等[19]采用基于密度泛函理论的粒子群优化算法,成功地确定了 Zinin 等[7]合成的立方类金刚石结构 BC_3(d-BC_3)的晶体结构,理论模拟该晶体结构的 X 射线衍射谱及拉曼光谱与实验结果完全吻合。研究结果表明,d-BC_3 的空间群为 $I\text{-}43m$,每个单胞中包含 16 个分子式

* **收稿日期**:2017-09-14;**修回日期**:2017-09-20

基金项目:国家自然科学基金(11647007);陕西省教育厅科学研究计划(17JK0041);宝鸡文理学院科研计划项目(ZK2017009)

作者简介:常少梅(1981—),女,学士,实验师,主要从事功能材料模拟研究. E-mail:csm7027@163.com

(formula units,f. u.),共 64 个原子,其理论计算的硬度为 62 GPa,与立方氮化硼的硬度相同,是潜在的超硬材料。

实验合成 d-BC_3 需要高温高压条件,尽管已经采用理论模拟的方法成功确定了其晶体结构,然而目前尚没有 d-BC_3 在高压下的晶格常数、力学性质和热力学性质的相关研究报道。本工作采用基于密度泛函理论的第一性原理方法,系统地研究超硬 d-BC_3 在高温高压条件下的晶格常数、力学性质和热力学性质。

1　计算方法

在结构优化和自洽计算过程中,全部使用基于密度泛函理论和平面波展开的 VASP(Vienna *Ab initio* Simulation Package)软件包[20]。电子的交换关联势能函数采用广义梯度近似(General Gradient Approximation,GGA)下的 PBE(Perdew-Burke-Ernzerh)交换关联泛函[21],电子与核之间的相互作用采用冻核近似的全电子投影缀加平面波(Projector Augmented Wave,PAW)赝势[22]描述,其中 B 和 C 的价电子分别为 $2s^2 2p^1$ 和 $2s^2 2p^2$。为了保证计算的可靠性和有效性,平面波截断能设置为 800 eV,布里渊区 k 点的选取采用 Monkhorst-Pack 网格方法,网格采样的间距为 0.3 nm^{-1}。系统总能收敛测试表明:上述设置能够有效地保证能量收敛到 1 meV/f. u. 量级。弹性常数的计算基于力收敛的弛豫结构,采用应力-应变方法。不同压力下的体弹性模量 B、剪切模量 G、杨氏模量 Y 由 Voigt-Reuss-Hill 近似[23]确定。d-BC_3 在高温高压下的热力学性质采用准简谐近似的 Debye 模型[24],该模型已经成功应用到许多材料的热力学性质计算中。

2　结果与讨论

2.1　晶格常数和物态方程

在零压条件下,d-BC_3 是类金刚石的立方结构,空间群为 I-43m(No. 217),其晶体结构如图 1 所示。弛豫 d-BC_3 结构得到其零压下的晶格常数 $a_0=b_0=c_0=0.73331$ nm,与文献[19]的结果($a_0=0.73330$ nm)几乎完全吻合,B 原子和 C 原子的分数坐标与文献[19]也符合得非常好,证明了所采用的计算方法的精确性和可靠性。零压条件下 d-BC_3 的密度 $\rho_0=3.16$ g/cm^3,略小于超硬的金刚石密度(3.53 g/cm^3)。对零压下的 d-BC_3 连续施加压力,加压范围为 0～100 GPa,间隔为 5 GPa,对加压条件下的 d-BC_3 进行结构弛豫,其依然保持空间群为 I-43m 的立方结构。图 2(a)给出了 d-BC_3 归一化的晶格常数 a/a_0 和密度 ρ/ρ_0 随压力的变化关系。

可以看到,随着外加压力的不断增大,d-BC_3 的晶格常数逐渐减小,晶格常数和压力之间基本呈现线性关系。尽管如此,当压力达到 100 GPa(100 万个大气压)时,d-BC_3 的晶格常数与零压下比较仅减小了 7%左右,说明 d-BC_3 具有优异的抗压缩能力,可以作为潜在的超硬材料。采用最小二乘法和二次多项式拟合,得到归一化的晶格常数 a/a_0 和压力 p(GPa)之间的解析关系,即

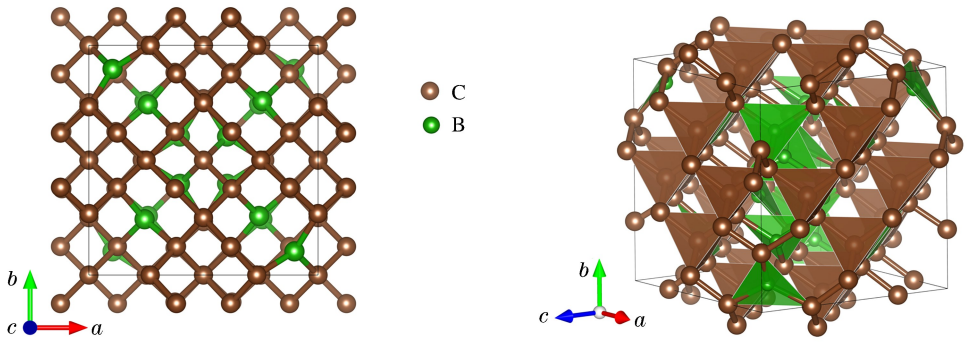

图 1　立方 BC_3 的晶体结构

Fig. 1　Crystal structure of cubic BC_3

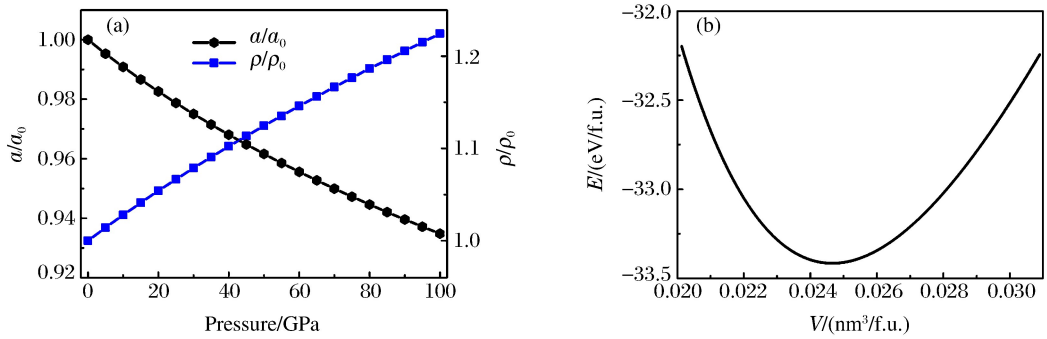

图 2　立方 BC_3 归一化晶格常数 a/a_0 和密度 ρ/ρ_0 随压力的变化关系(a)以及能量-体积物态方程(b)

Fig. 2　Pressure dependence of normalized lattice constants a/a_0 and density ρ/ρ_0(a), and the equation of state for cubic BC_3(b)

$$\frac{a}{a_0}=0.99941-8.71\times10^{-4}p+2.29\times10^{-6}p^2 \tag{1}$$

同时，由于 d-BC_3 具有优良的抗压缩性，随着压力的增加，其密度缓慢增大，直到压力增至 100 GPa 时，其密度仅仅比零压下的密度增大了 22%。

为了得到 d-BC_3 的物态方程，在负压力条件下，对 d-BC_3 的晶体结构连续地进行结构优化，提取各个压力点下的总能 E 和体积 V，整合正压力(0～100 GPa)条件下的总能 E 和体积 V 数据，根据三阶 Birch-Murnaghan 方程[25]即可拟合出 d-BC_3 的物态方程

$$E(V)=E_0+\frac{9V_0B_0}{16}\left\{\left[\left(\frac{V_0}{V}\right)^{\frac{2}{3}}-1\right]^3B_0'+\left[\left(\frac{V_0}{V}\right)^{\frac{2}{3}}-1\right]^2\left[6-4\left(\frac{V_0}{V}\right)^{\frac{2}{3}}\right]\right\} \tag{2}$$

式中：E_0、V_0、B_0 分别为零压下的总能、体积和体弹性模量，B_0' 为体弹性模量对压力的一阶导数。图 2(b)给出了采用三阶 Birch-Murnaghan 方程拟合得到的 d-BC_3 物态方程。拟合得到，零压下 d-BC_3 每个分子式的体积为 0.02466 nm^3，体弹性模量 B_0=341 GPa，体弹性模量对压力的一阶导数 B_0'=3.75。

2.2　力学性质

2.2.1　弹性常数

晶体的弹性常数是表征晶体弹性性质的物理量，反映晶体对外加应变的响应程度。对材料的晶体结构从相反方向上施加 6 组共计 12 个应变，自洽计算得到每个应变下的应力大小，然后利用广义胡克定律即可求得材料的弹性常数矩阵。对于立方晶系，其独立的 3 个弹性常数为 C_{11}、C_{12} 和 C_{44}。图 3 给出了 0～100 GPa 压力区间内 d-BC_3 的 3 个独立弹性常数随压力的变化关系。显然，随着压力的逐渐增大，C_{11}、C_{12} 和 C_{44} 呈现明显的增加。相比较而言，C_{11} 的斜率最大，说明 C_{11} 随着压力的增加变化幅度最大，因此 d-BC_3 沿 a、b、c 3 个主晶轴方向对应变的响应最明显。而 C_{44} 的斜率最小，说明 C_{44} 随着压力的增加变化最慢。根据 Born-Huang 弹性稳定性条件，立方晶系弹性稳定性条件为[26]

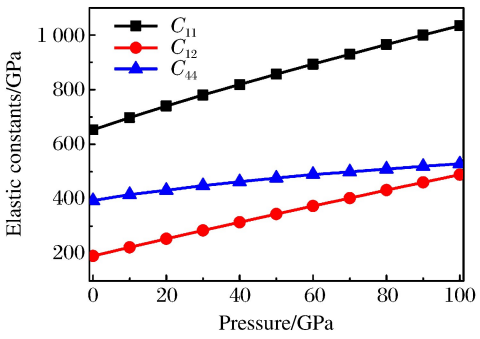

图 3　立方 BC_3 弹性常数随压力的变化关系

Fig. 3　Pressure dependence of elastic constants for cubic BC_3

$$C_{11}-C_{12}>0,\quad C_{11}+2C_{12}>0,\quad C_{44}>0 \tag{3}$$

显然，从 0 GPa 到 100 GPa，d-BC_3 一直满足 Born-Huang 弹性稳定性条件，说明 d-BC_3 在研究的压力范围内具有力学稳定性。

2.2.2　弹性模量

计算材料弹性模量的模型有 2 种：一种是 Voigt 模型，假设晶体的所有晶粒具有相同的应变，它反映材料刚度的上限；另一种是 Reuss 模型，假设晶体所有晶粒具有相同的应力，它反映材料刚度的下限。更为合理的方法是取 Voigt 模型和 Reuss 模型的算数平均值来计算材料的体弹性模量和剪切模量，即 Voigt-Reuss-Hill 近似[23]。对于立方晶系的晶体，Voigt 体弹性模量 B_V、Voigt 剪切模量 G_V、Reuss 体弹性模量 B_R 和 Reuss 剪切模量 G_R 分别定义为[27]

$$B_V = B_R = (C_{11} + 2C_{12})/3 \tag{4}$$

$$G_V = (C_{11} - C_{12} + 3C_{44})/5 \tag{5}$$

$$G_R = \frac{5(C_{11} - C_{12})C_{44}}{4C_{44} + 3(C_{11} - C_{12})} \tag{6}$$

由此可以得到 Voigt-Reuss-Hill 近似下的体弹性模量和剪切模量为

$$B = (B_V + B_R)/2 \tag{7}$$

$$G = (G_V + G_R)/2 \tag{8}$$

对于各向同性的材料，杨氏模量 Y 可以由体弹性模量和剪切模量表示为

$$Y = 9BG/(3B + G) \tag{9}$$

表 1 中列出了利用 0～100 GPa 的弹性常数计算得到的 d-BC_3 的体弹性模量、剪切模量和杨氏模量。从表 1 数据看出，压力为零时，d-BC_3 的体弹性模量的计算值为 345 GPa，与 2.1 节采用三阶 Birch-Murnaghan 方程拟合得到的结果(341 GPa)非常吻合。尽管与常见的超硬材料金刚石相比，d-BC_3 的体弹性模量、剪切模量和杨氏模量分别小了 20.0%、38.5%和 51.9%，但是 d-BC_3 的体弹性模量和剪切模量与超硬的立方氮化硼非常接近，说明其具有优异的抵抗外界应力的能力。随着压力的增大，d-BC_3 的体弹性模量、剪切模量和杨氏模量均逐渐增加，说明 d-BC_3 的刚度逐渐增大，对于一定的应力，它发生的弹性形变逐渐变小。从原子成键的角度分析可以得到，其主要原因是压力越大，d-BC_3 的晶格常数越小，其中 B—C 键和 C—C 键的键长越小，因此成键强度越大，导致 d-BC_3 抵抗外界应力的能力越强，因此，弹性模量随着压力的增加而增大。

表 1　不同压力下立方 BC_3 的体弹性模量、剪切模量和杨氏模量

Table 1　Bulk modulus, shear modulus, and Young's modulus for cubic BC_3 under pressure

Material	Pressure/GPa	B/GPa	G/GPa	Y/GPa
d-BC_3	0	345	318	730
	10	381	332	772
	20	416	343	807
	30	450	354	841
	40	483	363	870
	50	515	371	898
	60	547	379	923
	70	578	386	948
	80	610	393	971
	90	640	399	992
	100	671	405	1 012
c-BN[28]	0	376	390	
Diamond[29-30]	0	432	517	1 109

2.2.3　力学各向异性

晶体材料的各向异性对于材料的塑性形变、断裂行为和弹性不稳定性具有非常重要的影响。对于立方晶系的晶体，沿着任意[hkl]方向的杨氏模量可以写为[31]

$$Y^{-1}=s_{11}-\beta_1(\alpha^2\beta^2+\alpha^2\gamma^2+\beta^2\gamma^2) \tag{10}$$

式中：α、β、γ 表示拉伸方向的 3 个方向余弦；$\beta_1=2s_{11}-2s_{12}-s_{44}$，而 s_{11}、s_{12}、s_{44} 表示晶体的 3 个独立弹性柔顺系数，可以用立方晶体的弹性常数 C_{11}、C_{12} 和 C_{44} 表示

$$s_{11}=\frac{C_{11}-C_{12}}{C_{11}^2+C_{11}C_{12}-2C_{12}^2},\quad s_{12}=\frac{C_{12}}{C_{11}^2+C_{11}C_{12}-2C_{12}^2},\quad s_{44}=\frac{1}{C_{44}} \tag{11}$$

图 4 给出了 d-BC_3 杨氏模量各向异性的三维图形和二维投影图。从图 4 中可以看出，与超硬金刚石的杨氏模量各向异性相比较[32]，d-BC_3 的杨氏模量各向异性较大，主要由于 d-BC_3 的 B—C 键成键强度小于金刚石的 C—C 成键，因此各个方向的杨氏模量呈现出较大区别。计算得到 β_1 的取值小于零，故由(7)式可得，杨氏模量在主晶轴 a、b、c 方向取极大值，即 $Y_{max}=Y_{[001]}=Y_{[010]}=Y_{[100]}=1/s_{11}=1\,034$ GPa，而在主对角线方向取极小值，即 $Y_{min}=Y_{[111]}=3/(s_{11}+2s_{12}+s_{44})=697$ GPa。对于 d-BC_3，杨氏模量沿主要晶轴方向的大小顺序可以写为：$Y_{[111]}<Y_{[011]}<Y_{[001]}$。

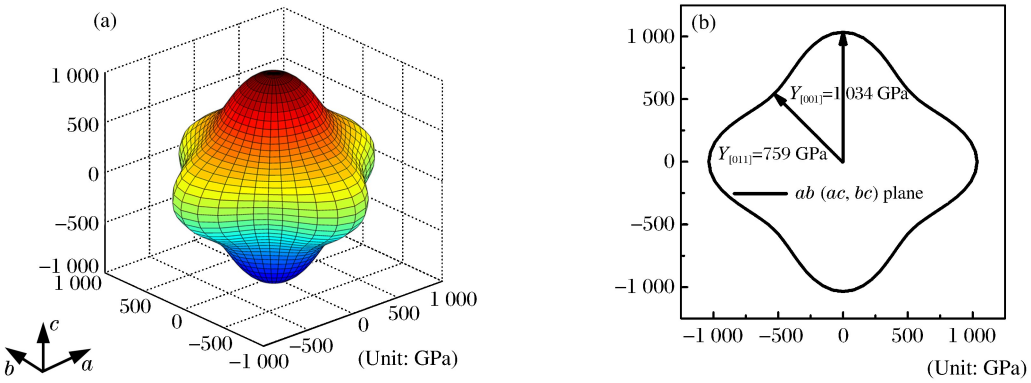

图 4　杨氏模量各向异性的三维图(a)和平面投影图(b)

Fig. 4　Three-dimensional plot (a) and the corresponding projection (b) of anisotropy of Young's modulus

2.3　热力学性质

文献[7,19]指出，d-BC_3 是在高温高压条件下合成的 BC_3 的亚稳态结构，因此非常有必要研究 d-BC_3 在高温高压条件下的物理性质。下面主要利用准简谐近似的德拜模型(Quasi-Harmonic Approximation Debye Model)[24]讨论高温高压条件下 d-BC_3 的热力学性质。根据 2.1 节计算得到的物态方程，采用准简谐近似的德拜模型，拟合得到 d-BC_3 在高温高压条件下的德拜温度和热容。采用文献[33]中德拜温度的计算公式可以得到，d-BC_3 在零压下的德拜温度 $\theta_D=1790$ K，而利用物态方程拟合得到的d-BC_3 在零压下的德拜温度 $\theta_D=1747$ K，两种方法的结果非常接近，说明本研究采用的准简谐近似的德拜模型是准确可靠的。图 5 给出了摩尔定容热容和摩尔定压热容随压力和温度的变化关系。从图5(a) 中看到：摩尔定容热容 c_V 随着温度的增加而增大；在温度一定的条件下，c_V 随着压力的增大而缓慢降低；当温度远大于德拜温度，即 $T\gg1747$ K 时，d-BC_3 的摩尔定容热容趋近于杜隆-珀蒂定律的结果99.72 J·mol^{-1}·K^{-1}(图 5(a)中虚线标示的位置)；当温度远小于德拜温度，即 $T\ll1747$ K 时，d-BC_3 的摩尔定容热容随着温度的增加而急剧增大，符合德拜 T^3 律。由图 5(b)可知：在一定的压力下，摩尔定压热容 c_p 随着温度的增加而增大，主要原因是原来被冻结的部分高频晶格振动模式在高温下对热容产生贡献；在温度一定时，摩尔定压热容 c_p 随着压力的增大而逐渐减小。

德拜温度是能量均分定理适用的最低温度。由图 5 可得，d-BC_3 的德拜温度随着温度的增加逐渐减小，说明温度的增加激发了更多的高频晶格振动模式，能量均分定理不再适用，因此导致 d-BC_3 的德拜温度减小。在一定温度下，d-BC_3 的德拜温度随着压力的增大而逐渐增大，主要原因是德拜温度反映材料内部原子的结合能大小，当压力增大时，原子之间的成键强度变大，使原子之间的结合能越大，因此提高了材料的德拜温度。

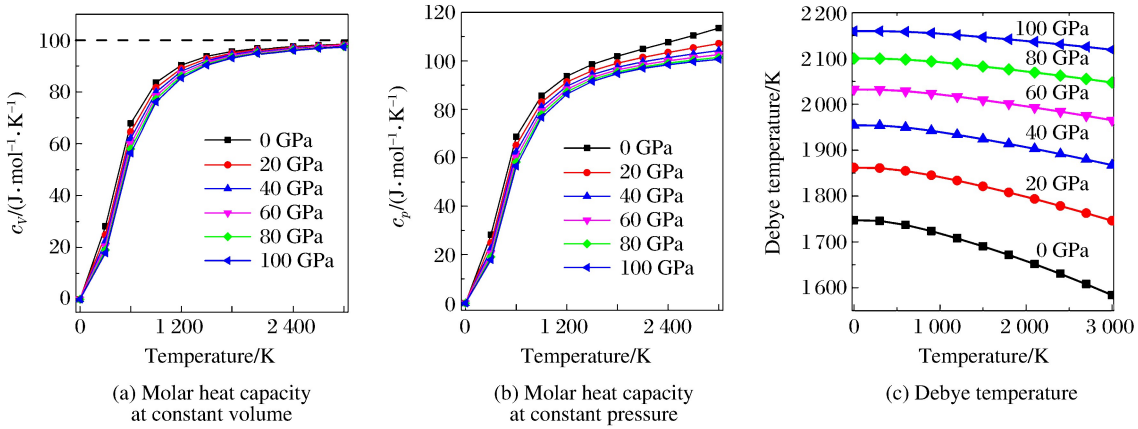

图 5　立方 BC_3 的摩尔定容热容 c_V、摩尔定压热容 c_p 和德拜温度随压力和温度的变化关系

Fig. 5　Molar heat capacity c_V, c_p and Debye temperature vs. pressure and temperature for cubic BC_3

3　结　论

采用密度泛函理论框架下的第一性原理方法，主要研究了常压和高压下立方 BC_3 的力学性质和热力学性质。通过晶格常数和力学性质的计算，说明常压下立方 BC_3 拥有较高的弹性常数和弹性模量，具有良好的不可压缩性能，是潜在的超硬材料。力学各向异性的计算结果表明，立方 BC_3 的杨氏模量的各向异性比金刚石更显著。根据准简谐近似的德拜模型，计算得到了立方 BC_3 的摩尔定容热容、摩尔定压热容和德拜温度随温度和压力的变化关系。计算结果说明，在高温高压条件下，立方 BC_3 的摩尔定容热容和摩尔定压热容随着温度的增加而变大，随着压力的增大而缓慢减小。德拜温度随着温度的增大逐渐减小，但随着压力的增大，其取值明显增加。

参考文献：

[1] HAINES J, LÉGER J M, BOCQUILLON G. Synthesis and design of superhard materials [J]. Annual Review of Materials Research, 2001, 31(1): 1-23.

[2] TIAN Y, XU B, ZHAO Z. Microscopic theory of hardness and design of novel superhard crystals [J]. International Journal of Refractory Metals and Hard Materials, 2012, 33: 93-106.

[3] NOVIKOV N V. Synthesis of superhard materials [J]. Journal of Materials Processing Technology, 2005, 161(1): 169-172.

[4] SOLOZHENKO V L, GREGORYANZ E. Synthesis of superhard materials [J]. Materials Today, 2005, 8(11): 44-51.

[5] NOVIKOV N V, DUB S N. Fracture toughness of diamond single crystals [J]. Journal of Hard Materials, 1991, 2(1): 3-11.

[6] SOLOZHENKO V L, DUB S N, NOVIKOV N V. Mechanical properties of cubic BC_2N, a new superhard phase [J]. Diamond and Related Materials, 2001, 10(12): 2228-2231.

[7] ZININ P V, MING L C, ISHII H A, et al. Phase transition in BC_x system under high-pressure and high-temperature: synthesis of cubic dense BC_3 nanostructured phase [J]. Journal of Applied Physics, 2012, 111(11): 114905.

[8] SOLOZHENKO V L, KURAKEVYCH O O, ANDRAULT D, et al. Ultimate metastable solubility of boron in diamond: synthesis of superhard diamondlike BC_5 [J]. Physical Review Letters, 2009, 102(1): 015506.

[9] SOLOZHENKO V L, ANDRAULT D, FIQUET G, et al. Synthesis of superhard cubic BC_2N [J]. Applied Physics Letters, 2001, 78(10): 1385-1387.

[10] BADZIAN A R. Superhard material comparable in hardness to diamond [J]. Applied Physics Letters, 1988, 53(25):2495-2497.

[11] CHUNG H Y, WEINBERGER M B, LEVINE J B, et al. Synthesis of ultra-incompressible superhard rhenium diboride at ambient pressure [J]. Science, 2007, 316(5823):436-439.

[12] GOU H, DUBROVINSKAIA N, BYKOVA E, et al. Discovery of a superhard iron tetraboride superconductor [J]. Physical Review Letters, 2013, 111(15):157002.

[13] CROWHURST J C, GONCHAROV A F, SADIGH B, et al. Synthesis and characterization of the nitrides of platinum and iridium [J]. Science, 2006, 311(5765):1275-1278.

[14] KUMAR N R S, CHANDRA S, AMIRTHAPANDIAN S, et al. Investigations of the high pressure synthesized osmium carbide by experimental and computational techniques [J]. Materials Research Express, 2015, 2(1): 016503.

[15] DOMNICH V, REYNAUD S, HABER R A, et al. Boron carbide: structure, properties, and stability under stress [J]. Journal of the American Ceramic Society, 2011, 94(11):3605-3628.

[16] GLASS C W, OGANOV A R, HANSEN N. Uspex-evolutionary crystal structure prediction [J]. Computer Physics Communications, 2006, 175(11):713-720.

[17] LYAKHOV A O, OGANOV A R, STOKES H T, et al. New developments in evolutionary structure prediction algorithm uspex [J]. Computer Physics Communications, 2013, 184(4):1172-1182.

[18] WANG Y, LÜ J, ZHU L, et al. CALYPSO: a method for crystal structure prediction [J]. Computer Physics Communications, 2012, 183(10):2063-2070.

[19] ZHANG M, LIU H, LI Q, et al. Superhard BC_3 in cubic diamond structure [J]. Physical Review Letters, 2015, 114(1):015502.

[20] KRESSE G, FURTHMÜLLER J. Efficient iterative schemes for *ab initio* total-energy calculations using a plane-wave basis set [J]. Physical Review B, 1996, 54(16):11169-11186.

[21] PERDEW J P, BURKE K, ERNZERHOF M. Generalized gradient approximation made simple [J]. Physical Review Letters, 1996, 77(18):3865-3868.

[22] KRESSE G, JOUBERT D. From ultrasoft pseudopotentials to the projector augmented-wave method [J]. Physical Review B, 1999, 59(3):1758-1775.

[23] HILL R. The elastic behaviour of a crystalline aggregate [J]. Proceedings of the Physical Society Section A, 1952, 65(5):349-354.

[24] OTERO-DE-LA-ROZA A, LUAÑA V. Gibbs 2: a new version of the quasi-harmonic model code. Ⅰ. robust treatment of the static data [J]. Computer Physics Communications, 2011, 182(8):1708-1720.

[25] BIRCH F. Finite elastic strain of cubic crystals [J]. Physical Review, 1947, 71(11):809-824.

[26] MOUHAT F, COUDERT F X. Necessary and sufficient elastic stability conditions in various crystal systems [J]. Physical Review B, 2014, 90(22):224104.

[27] WU Z, ZHAO E, XIANG H, et al. Crystal structures and elastic properties of superhard IrN_2 and IrN_3 from first principles [J]. Physical Review B, 2007, 76(5):054115.

[28] ZHANG R F, VEPREK S, ARGON A S. Anisotropic ideal strengths and chemical bonding of wurtzite BN in comparison to zincblende BN [J]. Physical Review B, 2008, 77(17):998-1002.

[29] WANG Y J, WANG C Y. Mechanical properties and electronic structure of superhard diamondlike BC_5: a first-principles study [J]. Journal of Applied Physics, 2009, 106(4):043513.

[30] ZHANG R F, LIN Z J, VEPREK S. Anisotropic ideal strengths of superhard monoclinic and tetragonal carbon and their electronic origin [J]. Physical Review B, 2011, 83(15):4400-4408.

[31] CAZZANI A, ROVATI M. Extrema of Young's modulus for cubic and transversely isotropic solids [J]. International Journal of Solids and Structures, 2003, 40(7):1713-1744.

[32] KLEIN C A. Anisotropy of Young's modulus and Poisson's ratio in diamond [J]. Materials Research Bulletin, 1992, 27(12):1407-1414.

[33] ZHENG B, ZHANG M, LUO H G. Pressure effect on structural, elastic, and thermodynamic properties of tetra-

gonal B_4C_4[J]. AIP Advances,2015,5(3):436-439.

Mechanical and Thermodynamic Properties for Cubic BC_3 under High Pressure

CHANG Shaomei

(*College of Physics and Optoelectronic Technology, Baoji University of Arts and Sciences, Baoji* 721016, *China*)

Abstract: The lattice constant and mechanical properties of cubic BC_3 under ambient and high pressure, including the elastic constants, the elastic modulus, and the mechanical anisotropy, were investigated using the first principle method in the framework of the density functional theory. The thermodynamic properties under high temperature and high pressure were calculated in terms of the quasi-harmonic Debye model. The results obtained show that the cubic BC_3 possesses a large elastic modulus and a high degree of anisotropy under ambient pressure. Under high pressure, the lattice constant, elastic constants, and elastic modulus of cubic BC_3 increase significantly. The results obtained from the thermodynamic calculations suggest that the cubic BC_3 has a large Debye temperature, and the molar heat capacity at constant volume and pressure exhibits obvious variation under high temperature and high pressure. Meanwhile, The Debye temperature of cubic BC_3 increases with the increase of pressure, but decreases with the increase of temperature.

Keywords: first principle; cubic BC_3; high pressure; mechanical properties; thermodynamic properties

高压物理学报
CHINESE JOURNAL OF HIGH PRESSURE PHYSICS

第 32 卷 第 2 期
2018 年 4 月

高 压 物 理 学 报
CHINESE JOURNAL OF HIGH PRESSURE PHYSICS

Vol. 32, No. 2
Apr., 2018

DOI: 10.11858/gywlxb.20170561

Crystal Structure and Stability of $LiAlH_4$ from First Principles*

ZHANG Yilong, CUI Man'ai, LIU Yanhui

(*Department of Physics, College of Science, Yanbian University, Yanji* 133002, *China*)

Abstract: The structural stability of $LiAlH_4$, a promising hydrogen storage material, under high pressure was researched using the *ab initio* pseudopotential plane wave method. It is found that the phase transition occurs at 1.6 GPa from the α-$LiAlH_4$ phase to the β-$LiAlH_4$ (space group $I2/b$) phase. This phase transition is identified as first-order in nature with volume contractions of 18%. Moreover, the analysis of the phonon dispersion curves suggests that phase transition is related to the phonon softening. Mulliken population analyses indicated that the ambient phase (α-$LiAlH_4$) is expected to be the most promising candidate for hydrogen storage.

Keywords: crystal structure; hydrogen storage materials; density functional theory; pressure-induced structural transition; electronic structure

CLC number: O521.23 **Document code**: A

Light metal complex hydrides are promising materials for solid-state hydrogen due to their gravimetric hydrogen density[1-5]. For example, lithium alanate ($LiAlH_4$) and sodium alanate ($NaAlH_4$) have theoretical hydrogen capacities of 10.6% and 7.5% (mass fraction), respectively. Hence, $LiAlH_4$ and $NaAlH_4$ could be viable candidates for practical usage as on-board hydrogen storage. However, a serious problem with these materials is their poor kinetics and lacking reversibility with respect to hydrogen absorption/desorption. Recent experimental evidences show that $LiAlH_4$ and $NaAlH_4$ release 7.9% and 5.6% (mass fraction) of H, respectively. This represents nearly 4 and 5 times more stored hydrogen than $LaNi_5$-based alloys which are currently used in nickel-based hydride batteries. However, it is difficult to accurately identify the positions of the hydrogen atoms by the high-pressure X-ray and neutron diffraction studies. Therefore, exploration of the phase stability and structures has attracted a great deal of attention.

Under ambient conditions, $LiAlH_4$ crystallizes at a monoclinic structure with a space group $P2_1/c$ (denoted as α-$LiAlH_4$). The structure consists of AlH_4 units separated by Li^+ ions, and the hydrogen atoms are arranged around the aluminum atoms in an almost regular tetrahedral configuration. On the theoretical side, the α-$LiAlH_4$ structure transforms into a new tetragonal β-$LiAlH_4$ structure (space group $I4_1/a$) at 2.6 GPa with a 17% volume contraction[6]. However, the neutron diffraction confirms

* **Received date**: 2017-04-05; **Revised date**: 2017-04-30

Foundation item: National Natural Science Foundation of China (11764043)

Biography: ZHANG Yilong(1998—), male, undergraduate, major in computational physics under high pressure. E-mail: 122696148@qq.com

Corresponding author: LIU Yanhui(1971—), female, Ph. D, professor, major in computational physics under high pressure. E-mail: yhliu@ybu.edu.cn

CUI Man'ai(1979—), female, master, lecturer, major in computational physics under high pressure. E-mail: macui@ybu.edu.cn

that the structure of the high pressure β-$LiAlD_4$ has a monoclinic space group $I2/b$[7]. It is determined that there is a reversible phase transition back to the α-$LiAlD_4$ with a slow release of pressure and cooling. Consequently, the Raman measurement confirmed that the ambient structure transform to the β-$LiAlH_4$ structure (space group $I2/b$) at 3 GPa[8], as well as the previously reported transition pressure between 2.2 and 3.5 GPa[9].

In this work, we report our results on the geometries and electronic structures of $LiAlH_4$ with pressure using the *ab initio* calculations. The total-energy calculations for the pressure-induced phase transition in $LiAlH_4$ were performed. The structural transition from α- to β-$LiAlH_4$ happened at 1.6 GPa. The full phonon dispersion curves were calculated, for the first time, to provide the evidence of phonon stability for pressured-induced phase transition. We also discussed the density of states and bond overlap populations about the two phases.

1　Computational Method

The calculations were performed within the density functional theory (DFT), using the Perdew-Burke-Ernzerh of generalized gradient approximation functional[10-12]. A plane-wave norm-conserving pseudopotential method[13] as implemented in the CASTEP code[14] was employed. We used the plane-wave kinetic-energy cutoff of 850 eV which was shown to give excellent convergence of the total energies and structural parameters. According to the Monkhorst-Pack method, k-point spacing smaller than 0.3 nm^{-1} was individually adjusted in reciprocal space to the size of each computational cell[15]. The optimization was performed, all forces on atoms were converged to be less than 0.1 eV/nm and all the stress components are less than 0.02 GPa. The tolerance in the self-consistent field (SCF) calculation was set to 10^{-6} eV/atom. The phonon frequencies were calculated by the direct approach, which is based on the first-principles calculations of the total energy, the Hellman-Feynman forces, and the dynamical matrix as implemented in the phonon packages[16-17]. Convergence test gave the use of 2×1×1 and 2×2×1 supercell in the phonon calculation.

2　Results and Discussions

We optimize the crystal structures allowing simultaneously variations of unit cell and atomic positions at selected pressures. The calculated lattice parameters of α-$LiAlH_4$ (space group $P2_1/c$) and β-$LiAlH_4$ (space group $I2/b$) are listed in Table 1, which also includes the experimental data for comparison[18]. For the α-$LiAlH_4$ phase, the deviations between our calculated results and the experimental values are less than 2%, which is sufficiently accurate. This strongly supports the choice of the pseudopotentials and GGA approximation for the current study. The theoretical generated pressure-volume curve (see Fig. 1) shows that the α-$LiAlH_4$ transforms to a monoclinic phase of β-$LiAlH_4$ with a volume contraction ($\Delta V/V$) of 18%, which suggests that this is a first-order phase transition. The

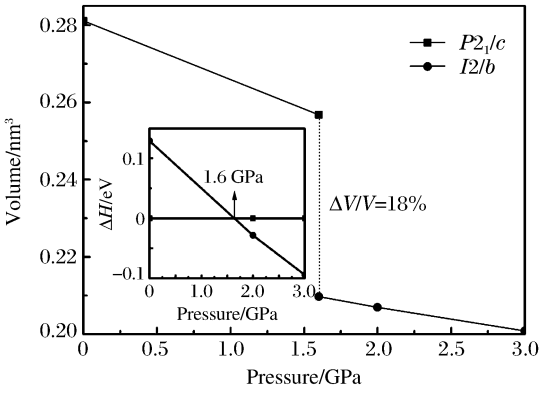

Fig. 1　Volume vs. pressure curves of α-$LiAlH_4$ and β-$LiAlH_4$ phases (Enthalpy difference (per formula unit) between α-$LiAlH_4$ and β-$LiAlH_4$ as a function of pressure is shown in the insert.)

huge volume contraction is consistent with the Raman scatting measurement and the other theoretical results[6,8]. In order to give a clear picture of the structural transition, the difference of the enthalpy (per formula unit) between the α-$LiAlH_4$ and β-$LiAlH_4$ phases as a function of pressure is shown in the insert of Fig. 1. It can be clearly seen that the β-$LiAlH_4$ phase becomes energetically more favourable than the α-$LiAlH_4$ phase above 1.6 GPa, which is the transition pressure from α-$LiAlH_4$ to β-$LiAlH_4$.

Table 1　Optimized structural parameters, atomic position parameters for the α-$LiAlH_4$ and the β-$LiAlH_4$ structures

Phase	Unit-cell dimensions	Atom coordinates
α-$LiAlH_4$ ($P2_1/c$)	a=0.485 1 nm(0.481 7 nm*) b=0.781 4 nm(0.780 2 nm*) c=0.773 2 nm(0.782 1 nm*)	Li:(0.585,0.459,0.829),(0.560,0.466,0.827)* Al:(0.159,0.204,0.938),(0.139,0.203,0.930)* H1:(0.193,0.102,0.766),(0.183,0.096,0.763)* H2:(0.377,0.371,0.986),(0.352,0.371,0.975)* H3:(0.254,0.082,0.119),(0.243,0.081,0.115)* H4:(0.822,0.268,0.882),(0.799,0.247,0.872)*
β-$LiAlH_4$ ($I2/b$)	a=0.445 2 nm b=0.445 9 nm c=1.010 2 nm β=89.978°	Li:(0,0.250,0.125) Al:(0,0.250,0.625) H1:(0.259,0.425,0.542) H2:(0.324,0.508,0.792)

Note: "*" represents experimental data from Ref. [18].

To investigate the dynamic stability, we calculated the phonon dispersion curves along some high-symmetry lines in the Brillouin zones (BZ) and the corresponding phonon density of states (DOS) for the $LiAlH_4$ structure. No imaginary frequency is observed throughout the whole BZ, indicating that the two novel phases are dynamically stable in the pressure region from this study. We also calculated the phonon dispersion curves at the phase transition pressure for the α-$LiAlH_4$ structure in Fig. 2. For comparison, the stability of phonon dispersion curves for the α-$LiAlH_4$ at 0 GPa are shown in Fig. 2(a). In Fig. 2(b), it is indicated that the phase transition should not be related to the pressure-induced phonon softening. The total and partial densities of states for the two phases are shown in Fig. 3. Analysis of the calculated electronic density of state reveals that the two phases exhibit a common insulating feature with a finite energy gap. The valence band (VB) in α-$LiAlH_4$ phase is split into two regions. Subsequently, the two peaks combine into one broader peak in the β-$LiAlH_4$ phase producing the broadening of VB under high pressure. This is originated from the shortened interatomic distance upon squeezing, for the VB region is mainly dominated by H 1s, and Al 2s, 2p states. It shows that the H and Al atoms become the directional covalent bonds within the AlH_4 tetrahedron or AlH_4 octahedron layers. The bottom of the conduction band just above the

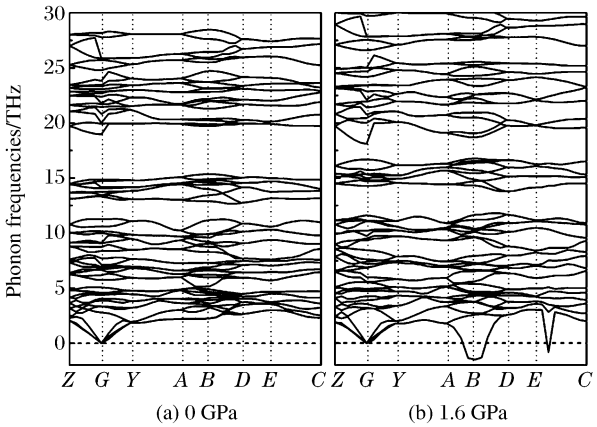

Fig. 2　Phonon dispersion relations and density of state in high-symmetry directions for the α-$LiAlH_4$ structure at 0 and 1.6 GPa

Fermi energy is composed of the Al $2s$, $2p$, Li $1s$, and H $1s$ states, which are consistent with the ionic bonding between the Li and the AlH_4 unit. We found more mixing of the s and p states for Al atom in the β-$LiAlH_4$ phase. Consequently, the electronic transition from the Al-s to -p state is related for the huge volume collapse during the α-$LiAlH_4$ to β-$LiAlH_4$ phase transition.

In order to better understand the bonding interactions between H, Al and Li atoms, we studied the Mulliken charges and the bond overlap population (BOP) P on the basis of Mulliken Populations in Table 2[19-20]. The scaled BOP (P^s) is defined in $P^s_{Al(Li)-H} = P_{Al(Li)-H}/L_{Al(Li)-H}$ with L representing the average bond length of Al—H or Li—H, respectively[21]. It is found that the P^s_{Al-H} value for the α-$LiAlH_4$ phase (0.506) is smaller than that of the β-$LiAlH_4$ phase (0.534) as the coordination number of Al (4) stays unchanged at the α-β transition. Previous studies have shown that the smaller the BOP, the lower the hydrogen desorption kinetic energy[22]. From this point of view, the current study suggests that the activation energy of the α-$LiAlH_4$ is lower than that of the β-$LiAlH_4$. The ambient phase of α-$LiAlH_4$ is expected to be the most promising candidate for hydrogen storage.

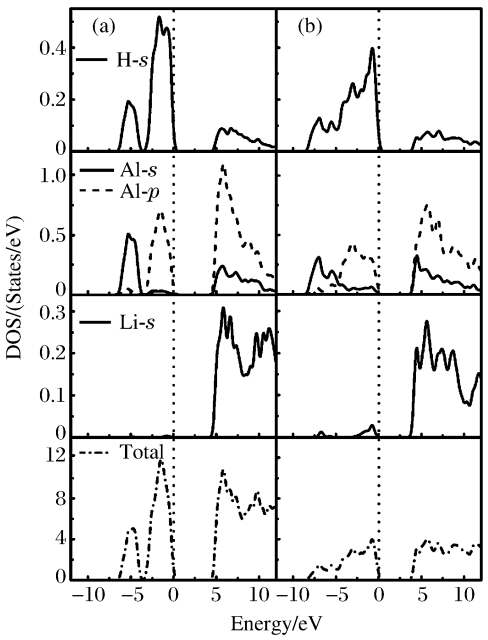

Fig. 3　Calculated total and partial electronic densities of states for α-$LiAlH_4$ structure at 0 GPa (a) and β-$LiAlH_4$ structure at 1.6 GPa (b) respectively

Table 2　Average net charges, bond length (L) and scaled bond overlap population (P^s) between H, Al, and Li atoms in the α-$LiAlH_4$ (at 0 GPa) and the β-$LiAlH_4$ (at 2.0 GPa) structures

Phase	Average net charge			L/nm		P^s	
	H	Al	Li	Al—H	Li—H	Al—H	Li—H
α-$LiAlH_4$	−0.48	0.64	1.29	0.1615	0.1886	0.506	0.019
β-$LiAlH_4$	−0.46	0.55	1.28	0.1628	0.2067	0.534	−0.063

3　Conclusions

We investigated the pressure-induced phase transformations in $LiAlH_4$ using the first-principles based on the density functional theory with the plane-wave basis. The structural transitions from α-$LiAlH_4$ to β-$LiAlH_4$ occurs at 1.6 GPa, accompanied with about 18% volume collapse, originating from the electronic transition of Al-s to -p states. The phase transition should be related to the pressure-induced phonon softening. The BOP analysis shows that the activation energy of the α-$LiAlH_4$ is smaller than that of the β-$LiAlH_4$. The α-$LiAlH_4$ is expected to be the most promising candidate for hydrogen storage.

Acknowledgements: This work was supported by the High Performance Computing Center of Yanbian University.

References:

[1] SCHLAPBACH L,ZÜTTEL A. Hydrogen-storage materials for mobile applications [J]. Nature,2001,414(6861):353-358.

[2] SCHÜTH F,BOGDANOVI Ć B,FELDERHOFF M. Light metal hydrides and complex hydrides for hydrogen storage [J]. Chemical Communications,2005,36(2):2249-2258.

[3] ZHU C Y,LIU Y H,DUAN D F. Structural transitions of $NaAlH_4$ under high pressure by first-principles calculations [J]. Physica B:Condensed Matter,2011,406(8):1612-1614.

[4] DILTS J A,ASHBY E C. Thermal decomposition of complex metal hydrides [J]. Inorganic Chemistry,1972,11(6):1230-1236.

[5] DYMOVA T N,ALEKSANDROV D P,KONOPLEV V N,et al. Spontaneous and thermal-decomposition of Lithium Tetrahydroaluminate $LiAlH_4$ — the promoting effect of mechanochemical action on the process [J]. Russian Journal of Coordination Chemistry,1994,20(4):279-285.

[6] VAJEESTON P,RAVINDRAN P,VIDYA R,et al. Huge-pressure-induced volume collapse in $LiAlH_4$ and its implications to hydrogen storage [J]. Physical Review B,2003,68:212101.

[7] PITT M P,BLANCHARD D,HAUBACK B C,et al. Pressure-induced phase transitions of the $LiAlD_4$ system [J]. Physical Review B,2005,72:214113.

[8] CHELLAPPA R S,CHANDRA D,GRAMSCH S A,et al. Pressure-induced phase transformations in $LiAlH_4$ [J]. The Journal of Physical Chemistry B,2006,110(23):11088-11097.

[9] TALYZIN A V,SUNDQVIST B. Reversible phase transition in $LiAlH_4$ under high-pressure conditions [J]. Physical Review B,2004,70:180101.

[10] HOHENBERG P,KOHN W. Inhomogeneous electron gas [J]. Physical Review B,1964,136(3):864-871.

[11] KOHN W,SHAM L. Self-consistent equations including exchange and correlation effects [J]. Physical Review A,1965,140(4):1133-1138.

[12] PERDEW J P,WANG Y. Accurate and simple analytic representation of the electron-gas correlation energy [J]. Physical Review B,1992,45(23):13244-13249.

[13] TROULLIER N,MARTINS J L. Efficient pseudopotentials for plane-wave calculations [J]. Physical Review B,1991,43(3):1993-2006.

[14] SEGALL M D,LINDAN P J D,PROBERT M J,et al. First-principles simulation:ideas,illustrations and the CASTEP code [J]. Journal of Physics:Condensed Matter,2002,14:2717-2744.

[15] MONKHORST H J,PACK J D. Special points for Brillouin-zone integrations [J]. Physical Review B,1976,13(12):5188-5192.

[16] PARLINSKI K,LI Z Q,KAWAZOE Y. First-principles determination of the soft mode in cubic ZrO_2 [J]. Physical Review Letters,1997,78(21):4063-4066.

[17] TOGO A,OBA F,TANAKA I. First-principles calculations of the ferroelastic transition between rutile-type and $CaCl_2$-type SiO_2 at high pressures [J]. Physical Review B,2008,78(13):134106.

[18] HAUBACK B C,BRINKS H W,FJELLVG H. Accurate structure of $LiAlD_4$ studied by combined powder neutron and X-ray diffraction [J]. Journal of Alloys and Compounds,2002,346(1):184-189.

[19] SEGALL M D,PICKARD C J,SHAH R,et al. Population analysis in plane wave electronic structure calculations [J]. Molecular Physics,1996,89(2):571-577.

[20] MULLIKEN R S. Electronic population analysis on LCAO-MO molecular wave functions [J]. The Journal of Chemical Physics,1955,23(10):1833-1840.

[21] HU C H,CHEN D M,WANG Y M,et al. First-principles investigations of the pressure-induced structural transitions in $Mg(AlH_4)_2$ [J]. Journal of Physics:Condensed Matter,2007,19:176205.

[22] WANG H,LI Q,WANG Y C,et al. High-pressure polymorphs of Li_2BeH_4 predicted by first-principles calculations [J]. Journal of Physics:Condensed Matter,2009,21:385405.

$LiAlH_4$ 晶体结构及稳定性的第一性原理研究

张艺龙，崔慢爱，刘艳辉

（延边大学理学院物理系，吉林 延吉　133002）

摘要：基于密度泛函理论的第一性原理赝势平面波方法，研究高压下三元碱金属氢化物 $LiAlH_4$ 的相变行为，分析了 $LiAlH_4$ 高压相变的物理机制。研究表明，在 1.6 GPa 时 $LiAlH_4$ 发生了相变，从 α-$LiAlH_4$ 转变为空间群为 $I2/b$ 的 β-$LiAlH_4$，相变时伴随 18％的体积坍塌，即一级相变。通过分析声子色散曲线得出，相变与声子软化有关。Millikan 布局分析表明，常压相（α-$LiAlH_4$）是很有潜力的储氢材料。

关键词：晶体结构储氢材料；密度泛函理论；压力诱导结构转变；电子结构

中图分类号：O521.23　　**文献标志码**：A

DOI:10.11858/gywlxb.20170630

压力作用下 Mg_2X(X=Si,Ge)相热力学性质的第一性原理研究*

张乐婷[1],赵宇宏[1],孙远洋[1],邓世杰[1],吉如意[1],韩培德[2]

(1.中北大学材料科学与工程学院,山西 太原 030051;
2.太原理工大学材料科学与工程学院,山西 太原 030024)

摘要:采用基于密度泛函理论的第一性原理方法,研究了压力作用下 Mg_2Si 和 Mg_2Ge 的结构、弹性和热力学性质。计算结果表明:0 GPa 压力作用下两者的晶格参数与实验值以及其他理论值吻合较好,且相对晶格常数 a/a_0 和晶胞体积 V/V_0 均随压力的增大而减小;在 0~25 GPa 压力作用下,Mg_2Si 和 Mg_2Ge 相体模量 B、剪切模量 G、杨氏模量 E 均随压力的增大而增大,材料的刚度和塑性均增强,当压力达到 15 GPa 时,材料由脆性转变为延性。最后借助准谐德拜模型和 Gibbs 软件,研究了温度与压力对 Mg_2Si 和 Mg_2Ge 的德拜温度、体模量、热容和热膨胀系数的影响。

关键词:第一性原理;Mg_2Si;Mg_2Ge;结构性质;弹性性质;热力学性质
中图分类号:O521.2;TG146.2 **文献标识码**:A

Mg_2X(X=Si,Ge)合金是一种很有实用前景、较具代表性的金属间化合物,储存丰富,其晶体结构呈 CaF_2 型(面心立方)。Mg_2X(X=Si,Ge)金属间化合物具有高电导率、低热导率、耐高温、耐腐蚀和高硬度等优点[1-4],在电子器件、能量器件等领域具有重要的应用前景。

目前对 Mg_2X 材料的研究很多,对于 Mg_2X 材料国内外也有很多的报道。Tani 等[5]采用第一性原理计算了 Mg_2Si 的光学性质。Jund 等[6]研究了 Mg_2Si 和 Mg_2Ge 不同缺陷下的能量,发现 Mg_2Ge 的形成能比 Mg_2Si 大 50%左右,并且缺陷在 Mg_2Ge 相中比在 Mg_2Si 中更加稳定。Ganeshan 等[7]研究了温度对 Mg_2X(X=Si,Ge,Sn,Pb)的弹性常数的影响,发现随着温度的上升,Mg_2X 的弹性常数下降。Wang 等[8]研究了 Mg_2Si 和 Mg_2Ge 的晶格动力学和热力学性质,获得了声子色散曲线和声子密度。张建新等[9]研究了铸态 Mg-Sn-Si 合金中 Mg_2X(Si,Sn)复合相的结构与特性。

虽然人们已经对 Mg_2X(X=Si,Ge)系列晶体做了大量研究,也得到了令人满意的结果,但在压力作用下,对其热力学性质缺乏研究。并且 Mg_2X(X=Si,Ge)材料常被广泛应用于高温高压的工作环境,所以研究 Mg_2X(X=Si,Ge)化合物在高温高压作用下的性质具有重大意义,同时第一性原理计算方法的快速发展,为此项工作的展开提供了很大的便捷。

本研究采用第一性原理计算方法,在压力(0~25 GPa)下,对 Mg_2X(X=Si,Ge)金属间化合物的结构性质、弹性性质和热力学性质进行研究计算。

1 计算方法与模型

计算过程采用基于密度泛函理论(DFT)[10]的 CASTEP 软件包及 Gibbs 软件来完成。晶体的波函数由平面波基组展开,截断能 E_{cut} 设定为 360 eV。电子交换关联能采用 GGA(Generalized Gradient Approximation)的 PBE(Perdew Burke Ernzerhof)[11]形式,势函数选用倒易空间的超软赝势 Ultrasoft[12]。

* **收稿日期**:2017-08-14;**修回日期**:2017-10-25
基金项目:国家自然科学基金(51774254,51774253,51701187,U1610123,51674226,51574207,51574206);山西省科技重大专项(MC2016-06)
作者简介:张乐婷(1992—),女,硕士研究生,主要从事材料的模拟计算研究. E-mail:1092720809@qq.com
通信作者:赵宇宏(1974—),女,博士,教授,主要从事计算机多尺度模拟研究. E-mail:zhaoyuhong@nuc.edu.cn

布里渊区[13]的积分计算通过 Monkhors-Pack 形式的高对称 k 点方法，倒易空间采用 0.05 nm^{-1} 的 k-point空间，k 点网格取 6×6×6。计算在最小化的快速 Fourier 网格上进行，首先采用 BFGS[14]算法，对所研究的晶胞模型进行几何优化，以获得最稳定的结构。进行自洽迭代 SCF 计算时，采用 Pulay 密度混合法解决电子弛豫，自洽收敛条件为：系统总能量在 1.0×10^{-5} eV/atom 内达到收敛，每个原子上的力低于 0.3 eV/nm，应力偏差低于 0.05 GPa，公差偏移低于 0.001 nm。

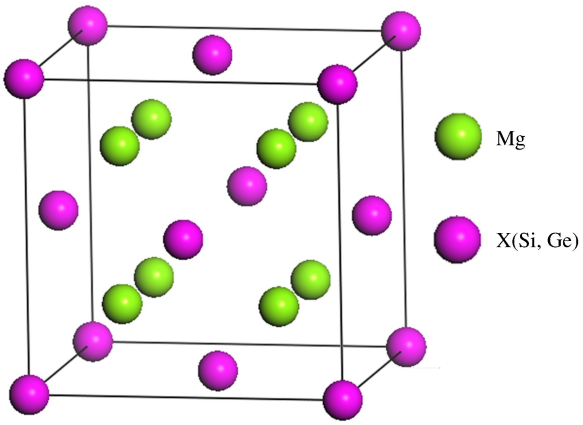

图 1　Mg_2X(X=Si,Ge) 的晶胞结构

Fig. 1　Crystal structure of Mg_2X (X=Si,Ge)

Mg_2Si 和 Mg_2Ge 都属于立方晶体结构，空间群为 $Fm\text{-}3m$，每个晶胞含有 12 个原子，原子空间排布如图 1 所示。在本研究中计算所采用的晶体结构为原胞形式，在 0 K 和 0 GPa 条件下使用 CASTEP 软件对晶胞进行晶体结构优化，计算得到的结构参数如表 1 所示。从表 1 中可以看出，计算所得晶格常数与实验值以及其他理论值很吻合。

表 1　Mg_2Si 和 Mg_2Ge 的晶格常数

Table 1　Equilibrium crystal parameters (a,c) of Mg_2Si and Mg_2Ge

Phase	This work		Calc.		Exp.	
	a/nm	c/nm	a/nm	c/nm	a/nm	c/nm
Mg_2Si	0.6351	0.6351	0.6387[4]	0.6387[4]	0.6338[15]	0.6338[15]
Mg_2Ge	0.4553	0.4553	0.6318[15]	0.6318[15]	0.6393[15]	0.6393[15]

2　结果与讨论

2.1　压力对晶体结构的影响

为了进一步研究压力对 Mg_2X(X=Si,Ge)晶体结构的影响，本研究以 5 GPa 为间隔，在 0～25 GPa 压力下对 Mg_2X(X=Si,Ge)进行压力测试，得到相对晶格参数 a/a_0 和相对体积 V/V_0 随压力的变化情况，如图 2 所示，其中 a_0 是 0 GPa 下的静态晶格常数，V_0 是 0 GPa 下的晶胞体积。

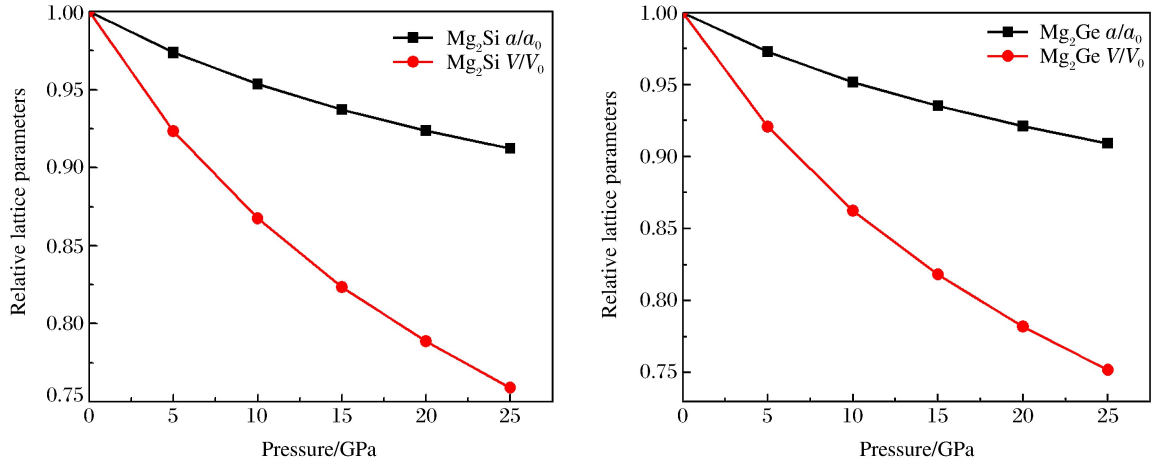

图 2　Mg_2Si 和 Mg_2Ge 的相对晶格参数(a/a_0)和相对体积(V/V_0)随外压力的变化

Fig. 2　Variations of relative lattice parameters (a/a_0) and relative unit cell volume (V/V_0) of Mg_2Si and Mg_2Ge with pressure

从图 2 中可以看出,晶格参数($a=b=c$)均随外压力的增大而逐渐减小,导致体积 V 和相对体积 V/V_0 也相应地减小。为了进一步了解 Mg_2Si 和 Mg_2Ge 的结构参数随静水压力的变化情况,对图 2 的曲线进行了拟合计算,得到了 Mg_2Si 和 Mg_2Ge 相的 a/a_0、V/V_0 与静水压力 p 的二元二次状态方程,(1)式和(2)式代表 Mg_2Si 相的状态方程,(3)式和(4)式表示 Mg_2Ge 相的状态方程。

$$a/a_0(Mg_2Si)=0.999\,29-0.005\,23p+7.107\,06\times10^{-5}p^2 \quad (1)$$

$$V/V_0(Mg_2Si)=0.997\,47-0.015\,16p+2.286\,78\times10^{-4}p^2 \quad (2)$$

$$a/a_0(Mg_2Ge)=0.999\,25-0.005\,43p+7.434\,76\times10^{-5}p^2 \quad (3)$$

$$V/V_0(Mg_2Ge)=0.997\,32-0.015\,70p+2.392\,37\times10^{-4}p^2 \quad (4)$$

图 3 给出了 $Mg_2X(X=Si,Ge)$在 0～25 GPa 下体积比 V/V_0 随压力变化情况,从图中可以看出,随着压力的增加,Mg_2Si 与 Mg_2Ge 的体积比均下降,当压力达到 25 GPa 时,两者的体积分别减少了 24.08%、24.80%,说明在压力作用下,Mg_2Ge 压缩性高于 Mg_2Si,且随着压力的增加,体积比降低速率逐渐缓慢,当压力增加到一定值时,压力对体积的影响会降低。

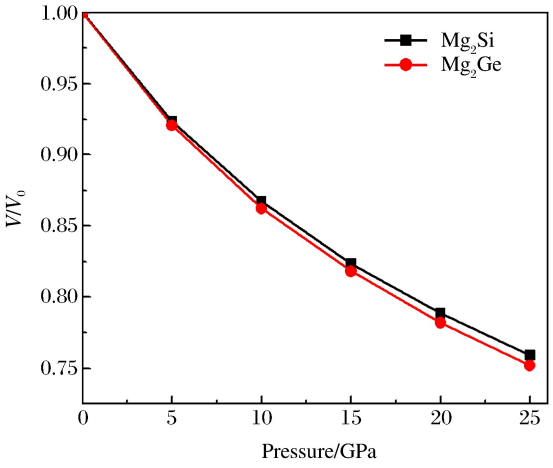

图 3　$Mg_2X(X=Si,Ge)$体积比 V/V_0 随压力变化关系

Fig. 3　Relative unit cell volume V/V_0 of Mg_2Si and Mg_2Ge with pressure

2.2　弹性性质

为了研究不同压力对弹性性质的影响,我们计算了 0～25 GPa 压力下 Mg_2Si 和 Mg_2Ge 的弹性常数,结果列于表 2。Mg_2Si 和 Mg_2Ge 均属于立方晶体,独立弹性常数为:C_{11}、C_{12}、C_{44},应满足力学稳定性条件[16]

$$C_{11}-C_{12}>0,C_{11}>0,C_{44}>0,C_{11}+2C_{12}>0 \quad (5)$$

从表 2 中可以看出,在 0 GPa 条件下计算得到的弹性常数(C_{ij}),与文献值吻合较好,通过观察不同压力下的弹性常数,发现其均满足弹性稳定性判断,说明两者均具有力学稳定性且没有发生相转变。

表 2　Mg_2Si 和 Mg_2Ge 的弹性常数

Table 2　Moduli of Mg_2Si and Mg_2Ge

Phase	p/GPa	C_{11}	C_{12}	C_{44}	B/GPa	G/GPa	E/GPa	G/B	υ
Mg_2Si	0	110.48	22.04	44.72	51.52	44.52	103.69	0.86	0.160
	Calc.[18]	115.21	22.14	43.11	53.163	44.48	104.34	0.84	0.173
	5	143.03	42.46	52.29	75.99	51.49	126.00	0.68	0.22
	10	158.67	52.89	61.20	88.15	57.87	142.45	0.66	0.23
	15	180.72	68.97	61.32	106.22	59.14	149.65	0.56	0.27
	20	200.49	85.12	64.56	123.58	61.81	158.93	0.50	0.27
	25	218.17	102.33	66.19	140.94	62.88	164.22	0.45	0.31
Mg_2Ge	0	105.80	21.18	41.90	49.39	42.07	98.29	0.85	0.17
	Calc.[19]	113.56	20.56	45.70	51.56	46.02	106.40	0.85	0.16
	5	140.74	45.52	55.27	77.26	52.21	127.83	0.68	0.22
	10	154.03	50.75	54.12	85.17	53.13	131.95	0.62	0.24
	15	175.03	68.13	59.79	103.76	57.25	145.07	0.55	0.27
	20	191.53	83.03	61.82	119.19	58.79	151.48	0.49	0.29
	25	209.82	101.41	63.24	137.54	59.62	156.29	0.43	0.31

通过弹性常数(C_{ij}),并利用 Voigt-Reuss-Hill (VRH)方法可以得到一系列弹性性质,如体积模量 B、剪切模量 G、弹性模量 E、泊松比 υ 等,对于 Mg_2Si、Mg_2Ge 合金相来说,其计算公式为

$$B=\frac{C_{11}+2C_{12}}{3} \tag{6}$$

$$G=\frac{3C_{44}+C_{11}-C_{12}}{5} \tag{7}$$

$$E=\frac{9BG}{3B+G} \tag{8}$$

$$\upsilon=\frac{3B-2G}{2(3B+G)} \tag{9}$$

从图 4 和表 2 中可以看出,体积模量 B、剪切模量 G 和杨氏模量 E 均随压力的增大而增大,说明压力的增加可以提升材料的抗体积变形能力、抗剪切应变能力和刚度。根据 Pugh 判断依据[17],剪切模量 G 和体模量 B 比值被用来分析材料的脆性和延性,划分节点的数值为 0.57。当 $G/B<0.57$ 时,材料表现为延性,当 $G/B>0.57$ 时,材料表现为脆性材料。在 0～10 GPa 之间,Mg_2Si 和 Mg_2Ge 均表现为脆性,当压力达到 15 GPa 时,Mg_2Si 和 Mg_2Ge 均开始表现出延性性质。泊松比 υ 数值越大,材料的塑性越好。随着压力的增加,泊松比 υ 均增大,说明材料的塑性均有所提升。

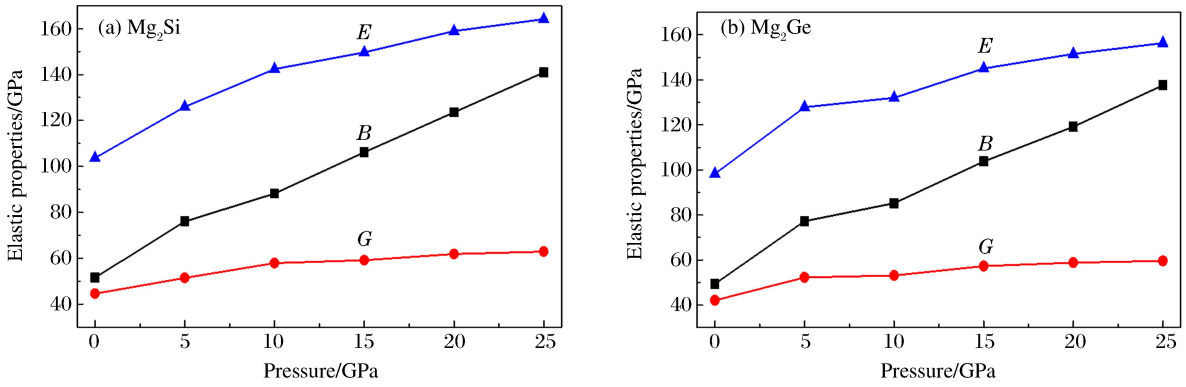

图 4　Mg_2Si 和 Mg_2Ge 的体积模量 B、剪切模量 G 和杨氏模量 E 随压力的变化情况

Fig. 4　Variation of bulk modulus B, shear modulus G, Young's modulus E of Mg_2Si and Mg_2Ge with pressure

2.3　热力学性质

Mg_2Si 和 Mg_2Ge 的热力学性质由第一性原理计算软件包 CASTEP 和 Gibbs 软件完成,本节研究了压力与温度对 Mg_2Si 和 Mg_2Ge 的德拜温度、体模量、热容的影响。

图 5 给出了 Mg_2Si 和 Mg_2Ge 德拜温度随温度和压力的关系。在 0 K 和 0 GPa 条件时,Mg_2Si 和 Mg_2Ge 的德拜温度分别是 551.72、438.57 K,与郭三栋[20]得到的数值 564、449 K 相对吻合。从图 5 可以看出,当温度处于 0～100 K 时,德拜温度变化不明显,当温度在 100～1 000 K 之间,德拜温度随着温度的升高而降低。对于压力而言,其对德拜温度的影响与温度相反。在 0～25 GPa 范围内随着压力的升高,德拜温度逐渐升高,并且压力对德拜温度的影响效果也随之降低。同时,从图 5 可以看出,

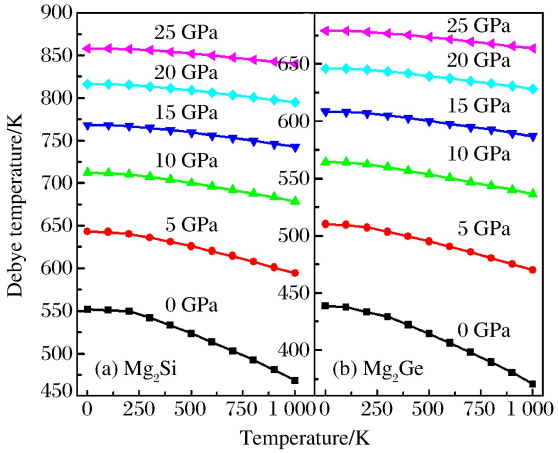

图 5　Mg_2Si 与 Mg_2Ge 德拜温度随温度与压强变化关系

Fig. 5　Debye temperature of Mg_2Si and Mg_2Ge at various pressures and temperatures

Mg_2Si 的德拜温度明显高于 Mg_2Ge，说明 Mg_2Si 化合物间原子作用力较大，膨胀系数较小。

体模量 B 通常用来表征在外加应力作用下，材料抵抗变形的能力。体模量 B 数值越大，抵抗变形能力越强。图 6 给出了 Mg_2Si 和 Mg_2Ge 体模量随温度和压力的变化情况。从图 6 可以看出，当温度在 0～100 K 范围内，体模量 B 变化微小，当温度在 100～1 000 K 时，体模量随温度的升高而降低。对于压力来说，在相同温度下，随着压力的增大，体模量逐渐增大。

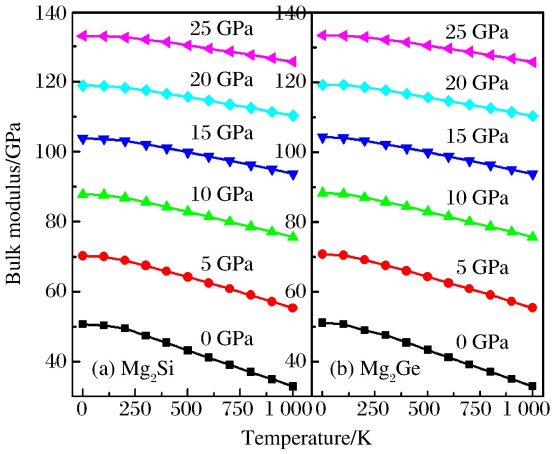

图 6　Mg_2Si 和 Mg_2Ge 体模量随温度和压力的变化

Fig. 6　Bulk modulus of Mg_2Si and Mg_2Ge at various pressures and temperatures

图 7 给出了 Mg_2Si 和 Mg_2Ge 的热容随温度和压力的变化情况，其中图 7(a)与图 7(b)分别表示等容热容 c_V、等压热容 c_p。从图中可以看出 $c_V \approx c_p$，当温度在 0～400 K 时，热容呈指数迅速升高，并且在温度为 0 K 时，二者均趋于零，这是由于德拜模型中的非简谐近似所致。当温度达到 600 K 以后，热容增长变缓，并且随着温度的升高，等压热容 c_p 继续增长，而等容热容 c_V 受到 Dulong-Petit 的限制，数值逐渐趋于平稳。此外，从图 7 中我们还发现压力对 c_V 和 c_p 的影响要明显小于温度对热容的影响。Mg_2Si 和 Mg_2Ge 的热容均随压力的增大而降低，并且 Mg_2Ge 热容值要高于 Mg_2Si。

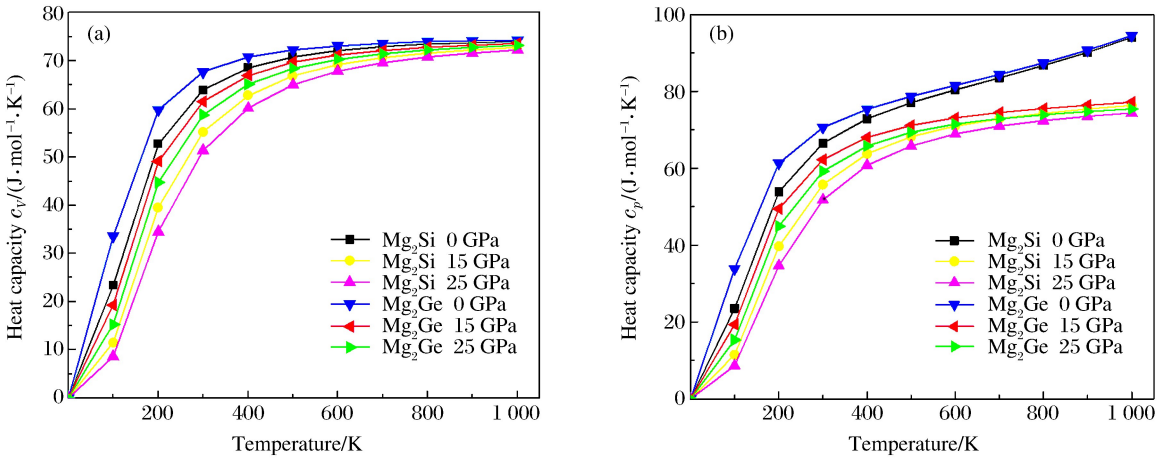

图 7　Mg_2Si 和 Mg_2Ge 热容随温度和压力的变化

Fig. 7　Heat capacity of Mg_2Si and Mg_2Ge at various pressures and temperatures

图 8 给出了 Mg_2Si 和 Mg_2Ge 的热膨胀系数随温度和压力的变化情况，从图中可以看出，Mg_2Si 和 Mg_2Ge 的热膨胀系数随温度的升高而增大，随着压力的增大逐渐降低。当温度在 0～300 K 时，热膨胀系数随温度呈线性增加，当温度超过 300 K 时，热膨胀系数增长变缓，说明温度对 Mg_2Si 和 Mg_2Ge 金属间化合物的热膨胀影响降低。从图 8 还可以看出，Mg_2Si 的热膨胀系数明显低于 Mg_2Ge，与德拜温度结果一致，说明 Mg_2Si 化合物的抗热震性能较好，Mg_2Si 化合物比 Mg_2Ge 化合物更能适应冷热交替温差较大的工作环境。

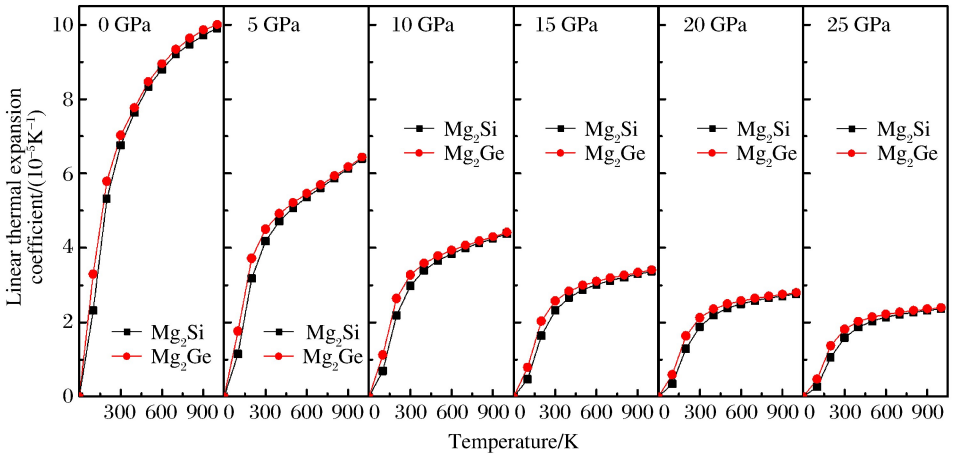

图 8　Mg_2Si 和 Mg_2Ge 热膨胀系数随温度和压力的变化

Fig. 8　Linear thermal expansion coefficient of Mg_2Si and Mg_2Ge at various pressures and temperatures

3　结　论

采用第一性原理方法计算了 Mg_2Si 和 Mg_2Ge 的弹性性质和热力学性质。

(1) Mg_2Si 和 Mg_2Ge 相对晶格常数 a/a_0 和晶胞体积 V/V_0 随压力的增大而减小，且在外部压力下 Mg_2Si 和 Mg_2Ge 相的 V/V_0 变化趋势很相似，在晶胞体积上具有相似的压缩率。

(2) 随着压力的增大，Mg_2Si 和 Mg_2Ge 相弹性常数 C_{ij}、体模量 B、剪切模量 G、杨氏模量 E 均增大，说明压力的增加可以提升材料的抗体积变形能力、抗剪切应变能力和刚度；在 0～10 GPa 之间，Mg_2Si 和 Mg_2Ge 均表现为脆性，当压力达到 15 GPa 时，Mg_2Si 和 Mg_2Ge 均开始表现出延性性质，同时随着压力的增加，材料的塑性均有所提升。

(3) 热力学性质表明，在 0～1000 K 下 Mg_2Si 和 Mg_2Ge 相的德拜温度和体模量均随温度的提升而降低，而热膨胀系数与之相反；对于压力(0～25 GPa)而言，在相同温度下，德拜温度和体模量均随压力的增大而增大，热膨胀系数与之相反。等容热容 c_V、等压热容 c_p 均随压力的增大而降低，Mg_2Ge 热容值高于 Mg_2Si，在高温下，等压热容 c_p 继续增长，而等容热容 c_V 受到 Dulong-Petit 的限制，热容值保持稳定。

参考文献：

[1]　陈茜，谢泉，杨创华，等. 掺杂 Mg_2Si 电子结构及光学性质的第一性原理计算 [J]. 光学学报，2009，29(1)：229-235.
CHEN Q，XIE Q，YANG C H，et al. First-principles calculation of electronic structure and optical properties of Mg_2Si with doping [J]. Acta Optica Sinica，2009，29(1)：229-235.

[2]　傅利，赵宇宏，杨晓敏，等. Mg-Al-Si-Ca 合金系金属间化合物的电子结构和力学性能的第一性原理计算 [J]. 稀有金属材料与工程，2014，43(11)：2733-2738.
FU L，ZHAO Y H，YANG X M，et al. First-principle calculation for electronic structure and mechanical properties of intermetallics in Mg-Al-Si-Ca Alloy [J]. Rare Metal Materials and Engineering，2014，43(11)：2733-2738.

[3] ZHANG J,FAN Z,WANG Y Q,et al. Microstructural development of Al-15 wt.% Mg_2Si *in situ* composite with mischmetal addition [J]. Materials Science and Engineering A,2000,281(1/2):104-112.

[4] 余本海,刘墨林,陈东. 第一性原理研究 Mg_2Si 同质异相体的结构、电子结构和弹性性质 [J]. 物理学报,2011,60(8):584-594.
YU B H,LIU M L,CHEN D. First principles study of structural,electronic and elastic properties of Mg_2Si polymorphs [J]. Acta Physica Sinica,2011,60(8):584-594.

[5] TANI J,KIDO H. First-principles and experimental studies of impurity doping into Mg_2Si [J]. Intermetallics,2008,16(3):418-423.

[6] JUND P,VIENNOIS R,COLINET C,et al. Lattice stability and formation energies of intrinsic defects in Mg_2Si and Mg_2Ge via first principles simulations [J]. Journal of Physics:Condensed Matter,2013,25(3):4469-4487.

[7] GANESHAN S,SHANG S L,WANG Y,et al. Temperature dependent elastic coefficients of Mg_2X (X=Si,Ge,Sn,Pb) compounds from first-principles calculations [J]. Journal of Alloys and Compounds,2010,498(2):191-198.

[8] WANG H,JIN H,CHU W,et al. Thermodynamic properties of Mg_2Si and Mg_2Ge investigated by first principles method [J]. Journal of Alloys and Compounds,2010,499(1):68-74.

[9] 张建新,高爱华,郭学锋,等. Mg-Sn-Si 合金中 Mg_2(Si,Sn)复合相的结构与性能研究 [J]. 物理学报,2013,62(17):483-488.
ZHANG J X,GAO A H,GUO X F,et al. Study on microstructure and poperties of Mg_2(Si,Sn) compound phase in Mg-Sn-Si magnesium alloy [J]. Acta Physica Sinica,2013,62(17):483-488.

[10] SHI D M,WEN B,MELNIK R. First-principles studies of Al-Ni intermetallic compounds [J]. Journal of Solid State Chemistry,2009,182(10):2664-2669.

[11] WANG F,SUN S J,YU B,et al. First principles investigation of binary intermetallics in Mg-Al-Ca-Sn alloy:stability,electronic structures,elastic properties and thermodynamic properties [J]. Transactions of Nonferrous Metals Society of China,2016,26(1):203-212.

[12] FAGAN S B,MOTA R,BAIERLE R J. Stability investigation and thermal behavior of a hypothetical silicon nanotube [J]. Journal of Molecular Structure,2001,539(1/2/3):101-106.

[13] CHADI D J. Special points for Brillouin-zone integrations [J]. Physical Review B,1977,16(4):5188-5192.

[14] FISCHER T H,ALMLOF J. General methods for geometry and wave function optimization [J]. Journal of Physical Chemistry,1992,96(24):9768-9774.

[15] TANI J,KIDO H. Lattice dynamics of Mg_2Si and Mg_2Ge compounds from first-principles calculations [J]. Computational Materials Science,2008,42(3):531-536.

[16] CAO Y,ZHU J C,NONG Z S,et al. First-principles studies of the structural,elastic,electronic and thermal properties of Ni_3Nb [J]. Computational Materials Science,2013,77(3):208-213.

[17] PUGH S F. Relations between the elastic moduli and the plastic properties of polycrystalline pure metals [J]. Philosophical Magazine,1954,45(367):823-843.

[18] 任玉艳,刘桐宇,李英民. Mg_2Si 金属间化合物的结构稳定性,热力学和力学性能的第一性原理计算 [J]. 中国科学:物理学 力学 天文学,2016,46(8):26-33.
REN Y Y,LIU T Y,LI Y M. First-principles calculation on structure stability,thermodynamic and mechanical properties of Mg_2Si intermetallics [J]. Scientia Sinica physica,Mechanica and Astronomica,2016,46(8):26-33.

[19] 常少梅. 压力作用下 Mg_2X(X=Sn,Ge,Si)晶体结构与弹性性质 [J]. 兰州理工大学学报,2012,38(5):168-171.
CHANG S M. Structural and elastic properties of Mg_2X (X=Sn,Gn,Si) under pressure [J]. Journal of Lanzhou University of Technology,2012,38(5):168-171.

[20] GUO S D. First-principles calculations of Mg_2X (X=Si,Ge,Sn) semiconductors with the calcium fluorite structure [J]. Journal of Semiconductors,2015,36(5):8-13.

Thermodynamic Properties of Mg_2X (X=Si, Ge) Phases under Pressure by First-Principles Calculations

ZHANG Leting[1], ZHAO Yuhong[1], SUN Yuanyang[1],
DENG Shijie[1], JI Ruyi[1], HAN Peide[2]

(1. *College of Materials Science and Engineering, North University of China, Taiyuan* 030051, *China*;
2. *College of Materials Science and Engineering, Taiyuan University of Technology, Taiyuan* 030024, *China*)

Abstract: The structural, elastic and thermodynamic properties of Mg_2Si and Mg_2Ge phases under pressure were calculated using the first-principles based on the density functional. The calculated results indicated that the lattice parameters under 0 GPa are fairly consistent with the experimental value and other theoretical data. The ratio of a/a_0 and V/V_0 decreased as the external pressure increases. An appropriate pressure (0-25 GPa) can improve their stiffness and plasticity because the bulk modulus B, shear modulus G, and Young's modulus E almost linearly increase with pressure. The brittleness of the material turns to ductility at 15 GPa. Finally, the effect of temperature and pressure on the Debye temperature, bulk modulus, heat capacity and linear thermal expansion coefficient was studied using the quasi-harmonic Debye model and Gibbs software.

Keywords: first-principles; Mg_2Si; Mg_2Ge; structural property; elastic property; thermodynamic property

高压物理学报

《高压物理学报》2018 年主题专刊名录

- 氢
- 高压物性实验研究
- 高压物性第一性原理计算
- 高压合成新材料
- 高压地球科学
- 静高压实验技术
- 动高压实验技术
- SHPB 实验技术
- 高压下材料和结构的力学性能和动态响应
- 界面不稳定性
- 高压科学应用——炸药起爆及安全性
- 高压科学应用——水下爆炸
- 高压科学应用——侵彻与防护
- 高压科学应用——破片
- 高压科学应用——爆燃及燃烧
- 高压科学应用——高压食品科学

★ 获取地址：http://www.gywlxb.cn/topics

2018年“高压物性第一性原理计算”主题专刊论文引用信息

☆ 李子鹤，刘超，马梦东，等. 新型超硬 C_5N 晶体结构及性能的第一性原理研究 [J]. 高压物理学报，2018，32(1)：010103.
LI Z H，LIU C，MA M D，et al. Structure and properties of novel superhard C_5N：a first-principles study [J]. Chinese Journal of High Pressure Physics，2018，32(1)：010103.

☆ 常少梅. 高压下立方 BC_3 的力学和热力学性质 [J]. 高压物理学报，2018，32(2)：021101.
CHANG S M. Mechanical and thermodynamic properties for cubic BC_3 under high pressure [J]. Chinese Journal of High Pressure Physics，2018，32(2)：021101.

☆ 张艺龙，崔慢爱，刘艳辉. $LiAlH_4$ 晶体结构及稳定性的第一性原理研究 [J]. 高压物理学报，2018，32(2)：021103.
ZHANG Y L，CUI M A，LIU Y H. Crystal structure and stability of $LiAlH_4$ from first principles [J]. Chinese Journal of High Pressure Physics，2018，32(2)：021103.

☆ 张乐婷，赵宇宏，孙远洋，等. 压力作用下 Mg_2X(X＝Si，Ge)相热力学性质的第一性原理研 [J]. 高压物理学报，2018，32(3)：032201.
ZHANG L T，ZHAO Y H，SUN Y Y，et al. Thermodynamic properties of Mg_2X (X＝Si，Ge) phases under pressure by first-principles calculations [J]. Chinese Journal of High Pressure Physics，2018，32(3)：032201.

征 稿 简 则

《高压物理学报》是我国高压物理领域唯一的专业性学术刊物。征稿内容包括：动态及静态高压技术，人工合成新材料，高温高压下材料的力、热、光、电、磁等特性以及物质微观结构的研究，动态及静态高压研究中的测试技术，高温高压下的相变，高温高压物态方程，高压地学，材料动态断裂，冲击和爆轰现象等。《高压物理学报》接受中、英文稿件。

自1987年创刊以来，《高压物理学报》取得了较大成就。2001年，《高压物理学报》被科技部和国家新闻出版总署评为“中国期刊方阵”双效期刊。国际主要检索系统Scopus、JSTChina、CA长期收录《高压物理学报》发表的文章。由北京高校图书馆期刊工作研究会和北京大学图书馆编著的《中文核心期刊要目总览》连续七版把《高压物理学报》列为物理学类核心期刊。

《高压物理学报》一贯秉承服务科学、服务读者、服务作者的办刊理念，慎重对待每一篇来稿，尊重作者劳动。优秀稿件享有快速发表通道，重大创新性成果可在1个月甚至更短时间内刊出。欢迎广大专家学者向《高压物理学报》投稿！

官方网站：www.gywlxb.cn
官方邮箱：gaoya@caep.cn
联系电话：0816-2490042